2D Lithospheric Imaging of the Delamerian and Lachlan Orogens, Southwestern Victoria, Australia from Broadband Magnetotellurics

Thesis submitted in accordance with the requirements of the University of Adelaide for an Honours Degree in Geophysics.

Hugh Merrett

October 2016

ABSTRACT

A geophysical study utilising the method of magnetotellurics (MT) was carried out across southwestern Victoria, Australia, imaging the electrical resistivity structure of the lithosphere beneath the Delamerian and Lachlan Orogens. Broadband MT (0.001-1000 Hz) data were collected along a 160 km west-southwest to east-northeast transect adjacent to crustal seismic profiling. Phase tensor analyses from MT responses reveal a distinct change in electrical resistivity structure and continuation further southwards of the Glenelg and Grampians-Stavely geological zones defined by the Yarramyljup Fault, marking the western limit of exploration interest for the Stavely Copper Porphyries. The Stawell and Bendigo Zones also show change across the Moyston and Avoca faults, respectively. Results of 2D modelling reveal a more conductive lower crust (10-30 Ωm) and upper mantle beneath the Lachlan Orogen compared to the Delamerian Orogen. This significant resistivity gradient coincides with the Mortlake discontinuity and location of the Moyston fault. Broad-scale fluid alteration zones were observed through joint analysis with seismic profiling, leaving behind a signature of low-reflectivity, correlating to higher conductivities of the altered host rocks. Isotopic analysis of xenoliths from western Victoria reveal the lithospheric mantle has undergone discrete episodes of modal metasomatism. This may relate to near-surface Devonian granite intrusions constrained to the Lachlan Orogen where we attribute the mid to lower crustal conductivity anomaly (below the Stawell Zone) as fossil metasomatised ascent paths of these granitic melts. This conductivity enhancement may have served to overprint an already conductive lithosphere, enriched in hydrogen from subduction related processes during the Cambrian. A predominately reflective upper crust exhibits high resistivity owing to turbidite and metasedimentary rock sequences of the Lachlan Orogen, representative of low porosity and permeability. Conductive sediments of the Otway Basin have also been imaged down to 3 km depth southwest of Hamilton.

KEYWORDS

magnetotellurics, electrical conductivity, Delamerian Orogen, Lachlan Orogen, lower crust, upper mantle, seismic reflectivity, southwest Victoria, Otway Basin

TABLE OF CONTENTS

LIST OF FIGURES

LIST OF TABLES

INTRODUCTION

The Earth's continental lithosphere comprises continental crust and the uppermost mantle, overlying a viscously deforming, weaker and hotter asthenosphere (Fowler, 2012). The internal structure of the continental lithosphere retains crucial evidence of its creation and orogenic processes through time (Jones, 1999). Geophysical interpretations of ancient orogenic systems have, to date, predominately been derived from deep seismic reflection profiling, capable of resolving structures to depths representative of the base of the crust (~40 km). This yields information on crustal evolution and deformational history, however the method is insufficient in resolving beyond sub-Moho depths. The large-scale tectonic processes of continental accretion (subduction and orogenic setting) physically influence the entire lithosphere and thus should be interpreted as a single interconnected system. Increasingly, magnetotellurics (MT) and seismic tomography methods have shown to be extremely effective tools to image much greater depths and provide significant insights into orogenic architecture not evident in seismic reflection surveys (i.e. Ledo et al., 2011; Selway, Heinson, & Hand, 2006). These methods are complementary to one another in that seismic parameters represent the bulk properties of the rock, whereas electromagnetic methods sense the presence of partially interconnected conducting phases, yielding bulk electrical conductivity (Everett, 2005).

The Tasman Orogenic System (Tasmanides) of eastern Australia represents the successive accretion of a number of Paleozoic orogenic belts onto the margin of Proterozoic Australia by subduction-related convergence at various stages throughout the Cambrian and Carboniferous (Glen, 2013). Two major orogenic belts of the southern Tasmanides reside in western Victoria; the Cambrian Delamerian Orogen and the Ordovician-Devonian Lachlan Orogen. Widespread agreement on the formation and evolution of these two Orogens (and more broadly the Tasman Orogenic System) remains elusive despite sustained research over many decades. Areas of ambiguity include the boundary between the Delamerian and Lachlan Orogens (i.e. Cayley, Korsch, Moore, et al., 2011; Cayley & Taylor, 2001;

Miller, Phillips, Wilson, & Dugdale, 2005), and the kinematics and geometry of the subduction zone(s) responsible for their accretion (Glen, 2013; Gray & Foster, 2004). This uncertainty can be attributed to lack of surface exposure, with over half of the Paleozoic basement beneath the southern Tasmanides masked by extensive Mesozoic and Cenozoic basin cover. Furthermore, post-accretionary tectonics have influenced the region over the past 200 Ma, largely obscuring the signature of ancient subduction accretion processes. However, a recent magnetotelluric study across central-western Victoria by Robertson, Taylor, Heinson, et al. (2015) reveal a west-dipping conductive anomaly below the Stawell Zone, inferred to represent a Cambrian subduction system. As such, this region is of interest for mineral exploration given Andean-style subduction margins are globally known to host porphyry copper deposits however, a lack of geological certainty and poor exposure has led to limited exploration activity.

A number of deep seismic reflection profiles have been collected predominately north of the study region (Cayley, Korsch, Moore, et al., 2011; Cayley, Korsch, Kennett, et al., 2011) providing crustal constraints on major faults and lithological units. The electrical resistivity structure of southwestern Victoria has never been studied in high resolution, with only two broad-scale (low resolution) surveys having been conducted (i.e. Aivazpourporgou, Thiel, Hayman, Moresi, & Heinson, 2015), and the Australian Lithospheric Architecture Magnetotelluric Program (AusLAMP) imaging the 3D resistivity structure of the entire state of Victoria (Duan, Taylor, Czarnota, Cayley, & Chopping, 2016). Seismic tomography studies have also been undertaken to delineate seismic velocity trends down to mantle depths including: teleseismic surface and body wave tomography (Rawlinson & Fishwick, 2012); teleseismic P-wave tomography (Rawlinson & Kennett, 2008); ambient noise tomography (Jiang, Yang, Rawlinson, & Griffin, 2016); teleseismic body wave tomography (Rawlinson, Kennett, Salmon, & Glen, 2015); and multiple inversion of teleseismic datasets (Rawlinson, Kennett, Vanacore, Glen, & Fishwick, 2011). These studies reveal a west to east transition from higher to lower wave speed velocities, representing a strong signature of the boundary between the Delamerian and Lachlan Orogens beneath the Stawell Zone (Figure 1). However, complex reworking

of the lithosphere from the breakup of Australia and Antarctica (90 Ma) and the Quaternary Newer Volcanic Province has masked the velocity contrast between the two Orogens at latitudes greater than 36^{o}S.

The tools to image the deep lithosphere are limited (i.e. magnetotellurics and seismic tomography) with xenolith isotopic data providing only appropriate geochemical constraints (Price, Gray, & Frey, 1997). The geophysical structure of the lithosphere is therefore key to unravelling its orogenic past. The electrical resistivity structure below southwestern Victoria is preserved as a signature within the crust and upper mantle, and is representative of the accretion of the Delamerian and Lachlan Orogens and subsequent tectonic events that have followed.

In this study, new broadband MT responses were collected at 31 stations along a 160 km ENE-WSW transect across southwestern Victoria to investigate the electrical resistivity structure of the Delamerian and Lachlan Orogens in greater detail. 2D inversion modelling and phase tensor analyses were conducted to resolve the location of the Delamerian-Lachlan boundary and continuation of a west-dipping paleo-subduction system further southwards.

TECTONIC AND GEOLOGICAL SETTING

The geology of southwestern Victoria comprises a complex interplay between the Tasman Orogenic System, Otway Basin and the Newer Volcanic Province. The Tasman Orogenic System (Foster & Gray, 2000; Glen, 2005) represents a continental-scale Neoproterozoic-Paleozoic system forming the eastern third of the present-day Australian continent. It consists of a series of accretionary orogens that

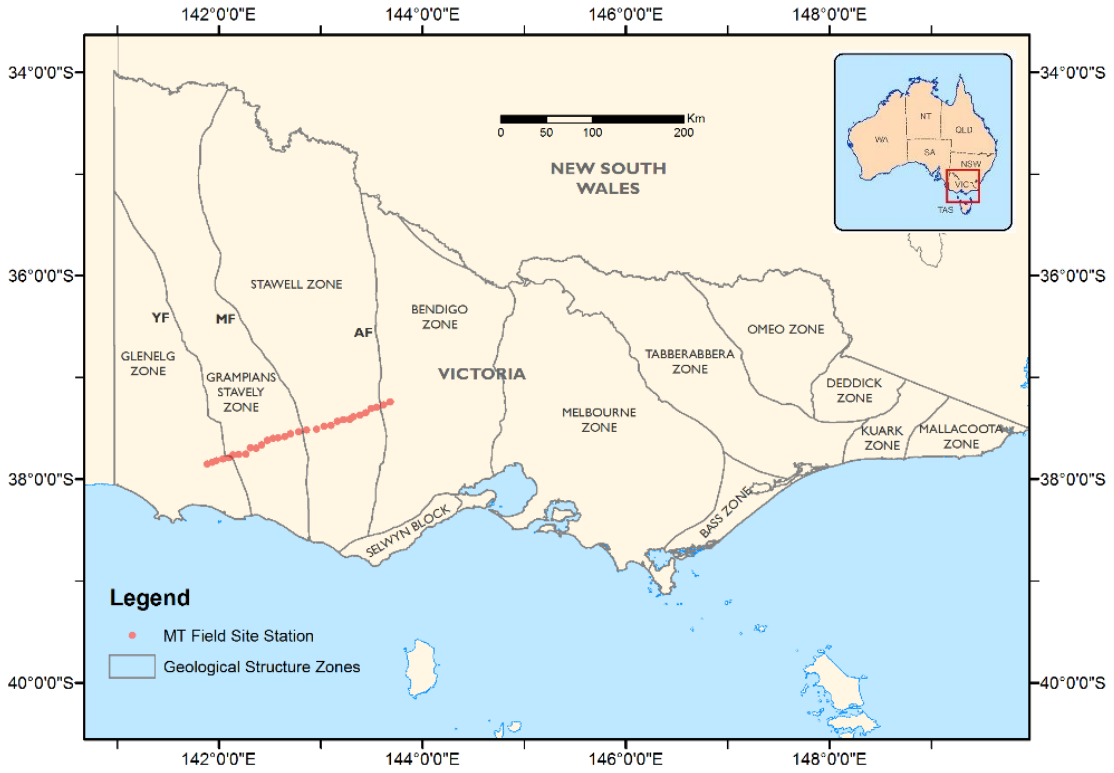

Figure 1: Study area overview map of Victoria. The acquired MT sites have been superimposed (red dots) which cross-cut the Glenelg, Grampians-Stavely, Stawell and Bendigo geological structure zones. These are bound by the location of the Yarramyljup (YF), Moyston (MF) and Avoca (AF) Faults. [Inset]: Location of the state of Victoria in reference to the Australian continent.

formed outboard of the Pacific margin of eastern Gondwana during the Early Cambrian through to the Middle Triassic (Glen, 2005). Through prolonged orogenesis, Paleozoic oceanic terranes and older micro-continental blocks were successively accreted onto the eastern margin of Precambrian Australia. Western Victoria encompasses the boundary between two major subdivisions of the Tasman orogenic system: The Cambrian Delamerian Fold Belt and the Ordovician-Devonian

Lachlan Fold Belt. The Delamerian Fold Belt has continental margin character with rift-related volcanics and sediments (Cayley, Korsch, Moore, et al., 2011). In South Australia, the Delamerian Orogen consists of Cambrian shallow to deep marine sedimentary rocks (Adelaide Rift Complex) deposited within a passive margin setting along the eastern margin of the Precambrian Gondwana craton (Cayley, Korsch, Moore, et al., 2011). Development of this margin occurred through the breakup of Rodinia (Proterozoic continent) and persisted until the Cambrian, changing into a convergent orogen (contractional orogenesis) with the arrival of the Delamerian Orogen. This initiated around 514 ± 3 Ma as a result of west-dipping subduction against the eastern margin of Gondwana, orogenesis ceased at approximately 490 ± 3 Ma due to rapid uplift, cooling, and extension (Foden, Elburg, Dougherty-Page, & Burtt, 2006). The Glenelg, Grampians-Stavely and Stawell geological structure zones represent the remnant back-arc, arc, and fore-arc subduction accretion terranes, respectively (Figure 1; Foden et al., 2006; Kemp, 2003; Miller et al., 2005).

The Lachlan Fold Belt formed outboard (eastwards) of the Delamerian Fold Belt soon afterwards from 485 to 340 Ma (Kemp, Hawkesworth, Collins, Gray, & Blevin, 2009) and includes four N-S trending geological zones in western and central Victoria including Stawell, Bendigo, Melbourne and Tabberabbera. The Lachlan Fold Belt is a region of deformed Early Paleozoic oceanic rocks accreted onto the eastern edge of the Delamerian Fold Belt during episodic orogenic cycles in the Ordovician-Silurian, Devonian and Carboniferous (Glen, 2005). The main exposed rocks within the western Lachlan Orogen are deep marine sediments intruded by oceanic volcanic rocks. Towards the culmination of this complex deformation, the geological zones of the Lachlan Orogen were intruded by significant volumes of post-tectonic granite (420-360 Ma; Chappell, White, & Hine, 1988). The granites locally post-date the deformation and occur as north-easterly trending linear features that cross-cut bedrock tectonic fabrics (Rossiter, 2003). Most of the granites are mafic I-types, particularly where the lower crust is thought to be Cambrian oceanic crust (Bendigo Zone).

Although the geology of western Victoria is largely controlled by these two major orogenic belts, they only extend to depths of 15-20 km within the crust (Cayley, Taylor, VandenBerg, & Moore, 2002) making interpretations of the composition of the lower crust difficult. Crustal models derived from seismic reflection data suggest the lower crust of the Stawell and western Bendigo zones is comprised of thickened oceanic crust (Cayley, Korsch, Moore, et al., 2011). Moreover, the lower crust beneath the Delamerian Orogen (Grampians-Stavely and Glenelg Zones) is thought to consist of mostly reworked Precambrian continental crust (Direen & Crawford, 2003).

The location and nature of Delamerian-Lachlan boundary is of debate with primary candidates for the boundary being the Avoca Fault (Glen, Scheibner, & VandenBerg, 1992) and the Moyston Fault (Cayley et al., 2002; VandenBerg, 1999). Miller et al. (2005) propose an alternative model suggesting the Moyston Fault overlies a reworked orogenic zone across the Stawell Zone containing elements of both the Delamerian and Lachlan Orogen.

Although the orogenic cycles giving rise to the Tasmanides were largely complete by 227 Ma (Glen, 2005), several subsequent tectonic events significantly affected the nature of the mantle beneath southeast Australia. This rifting and breakup of Australia and Antarctica in the late Jurassic (80-90 Ma) lead to the opening of the Tasman Sea and formation of the Otway Basin (Gaina et al., 1998). More recently, the Quaternary Basalts of the Newer Volcanic Province (NVP) overlie Paleozoic basement rocks of the Delamerian and Lachlan Orogens and Otway Basin sediments in the south (Lesti, Giordano, Salvini, & Cas, 2008). The extensive intraplate volcanic field covers an area of 19,000 km^2 with eruptions spanning 4.5 Ma to 5 ka (Boyce, 2013). Volcanism has been considered as simple and short-lived (monogenetic) with mechanisms for melting of the source magma remaining unclear, with theories relating to rifting, hotspot and mantle-plume activity, and edge-driven mantle convection (Boyce, Nicholls, Keays, & Hayman, 2014).

MAGNETOTELLURIC THEORY

Magnetotellurics (MT) is a passive electromagnetic (EM) method sensitive to electrical resistivity contrasts within the Earth from the near surface down to the mantle transition zone (410km) (Simpson & Bahr, 2005). The MT method utilises naturally occurring geomagnetic variations as a source for EM induction in the Earth. The electrical resistivity structure is obtained through measuring orthogonal components of natural electric and magnetic fields at the surface.

MT source signals are generated at high frequencies from global lightning discharges (> 10 Hz) and at low frequencies (< 10 Hz) by the interaction of the solar plasma with the Earth's magnetic field (ionosphere and magnetosphere) (Chave & Jones, 2012). These high and low frequency signals generate time-varying electromagnetic waves that penetrate the Earth.

A measure of the penetration depth (or skin depth) of diffusing EM fields into the Earth before becoming attenuated depends on the bulk resistivity of the medium and period of the signal, which is given by:

$$\delta(T) = \sqrt{\frac{T\rho}{\pi\mu}} \tag{1}$$

where the depth to which EM waves penetrate is given by the skin depth $\delta(T)$ in metres such that the amplitude of the EM fields are reduced to e^{-1} (or 37%) of their original amplitude at the surface for a given period (T). ρ represents the resistivity of the medium (Ωm) and μ is the magnetic permeability of free space ($\mu = 4\pi \times 10^{-7} Hm^{-1}$). Hence, the equation can be simplified to:

$$\delta(T) \approx 500\sqrt{T\rho} \tag{2}$$

Thus, greater signal penetration within the Earth is achieved with longer periods, and in more resistive terranes.

The relation between the electric (E) and magnetic (H) fields is described by the impedance tensor (Z) which is given by $E = ZH$, or in matrix form:

$$\begin{pmatrix} E_x \\ E_y \end{pmatrix} = \begin{pmatrix} Z_{xx} & Z_{xy} \\ Z_{yx} & Z_{yy} \end{pmatrix} \begin{pmatrix} H_x \\ H_y \end{pmatrix} \quad (3)$$

The impedance tensor can be simplified for 1D cases where $Z_{xx} = Z_{yy} = 0$ and $Z_{xy} = -Z_{yx} = Z$ for a purely 1D resistivity structure. For 2D electrical resistivity structures, the impedance tensor can be rotated to the geoelectric strike and separated into two independent modes through the elimination of Z_{xx} and Z_{yy}:

$$Z = \begin{pmatrix} 0 & Z_{xy} \\ Z_{yx} & 0 \end{pmatrix} \quad (4)$$

These modes are referred to as the transverse electric (TE) and transverse magnetic (TM) modes. The TE mode has electric fields parallel to strike with induced magnetic fields perpendicular to strike and in the vertical plane. Conversely, the TM mode has magnetic fields parallel to strike with induced electric fields perpendicular to strike and in the vertical plane (Simpson & Bahr, 2005).

Phase Tensor Ellipse

The phase (ϕ_{ij}) of the impedance element (Z) describes the phase shift between the recorded electric and magnetic field components (Chave & Jones, 2012). In this study, the phase tensor is represented in figures by an ellipse, where orientations of the phase tensor reflect lateral gradients in the resistivity structure (Caldwell, Bibby, & Brown, 2004).

The principal components of the phase tensor indicate the horizontal directions of maximum (Φ_{max}) and minimum (Φ_{min}) induction current through the use of an ellipsoid (Caldwell et al., 2004). The maximum induction direction is represented by the maximum axis of the ellipsoid, and is orientated in the direction of highest conductivity.

Phase angles Φ_{max} and Φ_{min} are a measure of ellipticity (ε);

$$\varepsilon = \frac{|\Phi_{max} - \Phi_{min}|}{\Phi_{max} + \Phi_{min}} \tag{5}$$

where equal Φ_{max} and Φ_{min} values represent a circle signifying conductivity structure varies only with depth (1D) (Figure 2a). A low minimum phase angle indicates high ellipticity (i.e. deviation from a circle) and illustrates 2D structure, given the maximum principal axis of the phase tensor ellipse are aligned parallel or perpendicular to the regional geoelectric strike (Figure 2b).

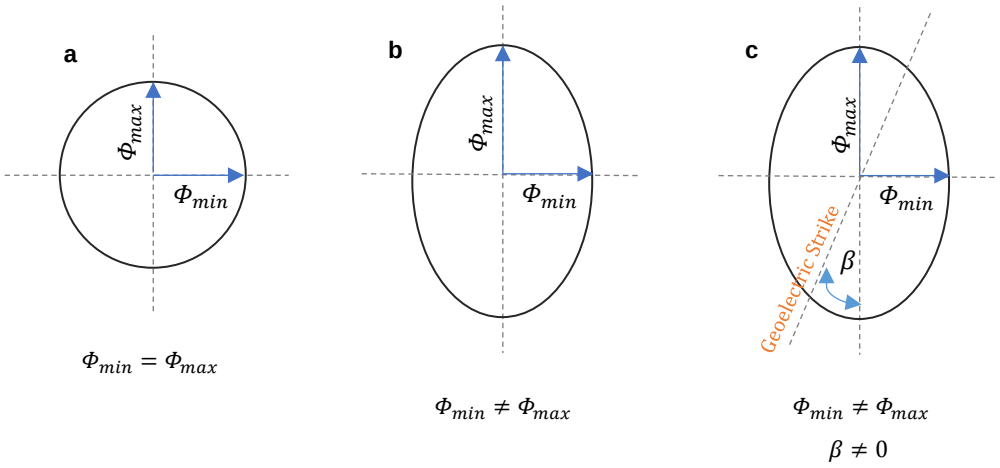

Figure 2: Schematic illustration of the phase tensor ellipse properties defining **a.** 1D, **b.** 2D and **c.** 3D electrical resistivity structure.

Skew (β) of the phase tensor is a measure of 3D symmetry, where asymmetric tensors contain a skew angle greater than 0^o (Bibby, Caldwell, & Brown, 2005). The difference between the geoelectric strike and the direction of maximum conductivity is referred to as the skew angle, where conductivity structure is 3D (Figure 2c). Ellipses can be shaded by minimum phase angle, where angles greater than 45° indicate a decrease in resistivity with depth, and angles less than 45° represent an increase in resistivity with depth (see Figure 6).

MAGNETOTELLURIC DATA

Field-Site Planning

Acquisition of high-quality MT data is challenging due to its reliance on the highly variable strength of natural electromagnetic excitation (Ritter et al., 1998). In addition, unnatural (artificial) electromagnetic sources often generate coherent large-amplitude signals that are superimposed. These artificial sources are caused by human activity and arise from main power supplies (power lines), electric fences, electric railways and radar/radio transmitters (Szarka, 1988).

To minimise cultural noise, Google-Earth satellite imagery in combination with Google Street View was used to conduct detailed site planning prior to field deployment to ensure the positioning of stations was suitable. Sites were positioned at least 500 m from houses, major roads, train lines and more than 1 km from power lines.

Data Acquisition

Broadband MT data were collected during June 2016 at 31 stations along a 160 km northeast-southwest transect across southwestern Victoria, Australia (Figure 3). With approximately 5 km station spacing, data was recorded at a frequency of 1000 Hz for a duration of 20-40 hours using AuScope equipment. Each station recorded two components of the electric field (E_x, E_y) and magnetic field (H_x, H_y) at the Earth's surface in orthogonal directions (x geomagnetic north-south and y geomagnetic east-west).

The electric field was recorded using non-polarising porous $PbCl_2$ electrodes oriented in an L-shaped configuration (north-south/east-west). The electrodes were buried vertically ensuring good contact with the ground (soil), then connected via 40-50 m cables to a data logger storing the measured signal. Parallel with the alignment of the electrodes, the magnetic field was recorded using two orthogonal (1.5 m ferrite core LEMI-120) coils that were buried to eliminate noise arising from

wind motion. Recording instruments were time synchronised using GPS, to enable more reliable data correlation. In addition, at least 3 stations recorded simultaneously for remote referencing in order to reduce electromagnetic noise (Gamble, Goubau, & Clarke, 1979).

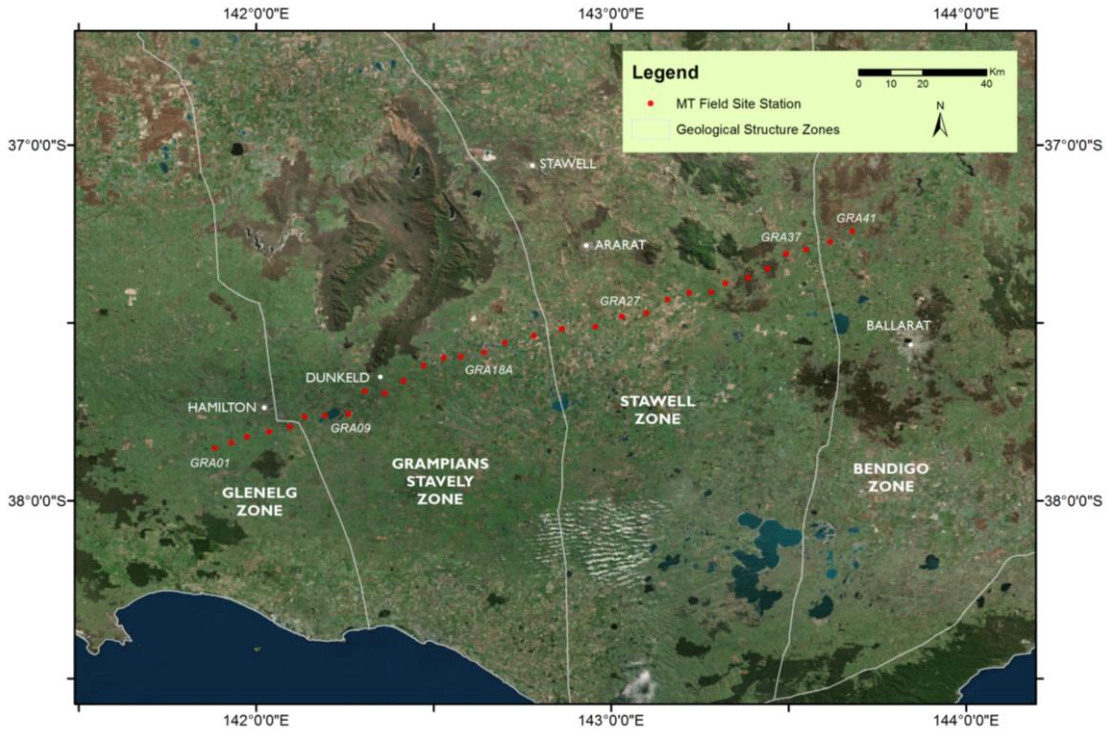

Figure 3: Acquired MT site locations (red dots) along the southwest Victoria transect. Only a select number of sites are labelled (i.e. GRA01, GRA09). Geological structure zones N-S trending (white lines) and major towns (white dots) within the study region also shown.

Data Processing

The raw time-series data were visually inspected to select proper segments for data processing. To extract the frequency content of the time series of the electric and magnetic fields for each site, the robust remote referencing code 'BIRRP' (Bounded Influence, Remote Reference Processing; Chave & Thomson, 2004) was used, enabling the application of Fourier transforms to transfer the time series into the frequency domain. The raw broadband data (1000 Hz) were decimated to obtain 10 Hz data and combined using transfer functions into 4 and 40 hour blocks. During processing data were rotated relative to the geomagnetic declination angle (~10° NNE) rotating the impedance tensor elements to the geographical coordinate

system (x representing geographic north, y representing geographic east). Lastly, a notch filter was applied to all stations to remove cultural noise at frequencies of 50, 150 and 250 Hz. The resultant output was an EDI file for each site containing information regarding the impedance tensor in the frequency domain.

The quality of the data across the processed frequency range was assessed based on apparent resistivity and phase coherence output plots generated by BIRRP, with noisy station data windows discarded and a new time window processed. Coherency values compare the electric response with the magnetic response and provided a good numerical indication of data quality. Remote referencing greatly improved the signal to noise ratio with the overall recorded data quality deemed adequate. Coherency values greater than 0.8 were observed for most frequencies, except within the dead band (0.1-10 Hz), where there is a markedly lower signal strength (Chave & Thomson, 2004).

Two sites were deemed unsuitable to be included for further MT analysis due to the contamination of high levels of electrical interferece from electric fencing (GRA01) and instrument failure (GRA41; inadequate recorded signal).

PRE-INVERSION ANALYSIS

MT data analysis was performed using two techniques; (1) the magnetotelluric phase tensor as described by Caldwell et al. (2004) and (2) the magnetotelluric ellipticity criterion by Becken and Burkhardt (2004). These methods were used to investigate strike, dimensionality and broad-scale resistivity trends of the dataset in order to determine whether two-dimensional modelling was deemed appropriate (i.e. is the assumption of two dimensionality fulfilled for stations throughout the recorded period range, and under what geoelectric strike is two-dimensionality optimized).

Geoelectric Strike

The geoelectric strike describes the preferred direction of current flow. In a two-dimensional Earth conductivity only varies in two directions: along the vertical axis (with depth) and along one horizontal axis. Along the remaining horizontal axis, conductivity remains constant and is referred to as the geoelectric strike (Naidu, 2012). In an ideal 2D case, if the impedance tensor is illustrated in a coordinate system with axes parallel and perpendicular to the geoelectric strike direction, the diagonal elements of the MT impedance tensor are zero. In practice however, there is no rotation such that both diagonal elements are precisely zero (Groom & Bailey, 1989).

Analysis of strike direction was conducted using the ellipticity criterion method as described by Becken and Burkhardt (2004). Rose diagrams were used to depict the average strike direction over selected period bands ranging from 0.0064 to 2184 s (Figure 4). Differences in strike direction with depth were observed with increasing period, suggesting changes in resistivity structure with depth.

Shorter periods (< 0.1 s) representative of the upper crust show no clear alignment of geoelectric strike and are scattered in all directions, typical of a one-dimensional environment where there is no clear polarisation of near surface electric currents (Figure 5a). For mid-upper crustal depths (periods 1-10 s) two dominant geoelectric strikes are observed, N60°E and N30°W. A 90° ambiguity of strike is apparent at longer periods (> 10 s) with reasonable agreement of 45° and 315° (Figure 4d, e). Analysis with regional geology, gravity and magnetic images delineate a dominant NW-SE geological strike enabling the 90° ambiguity to be resolved (Figure 6).

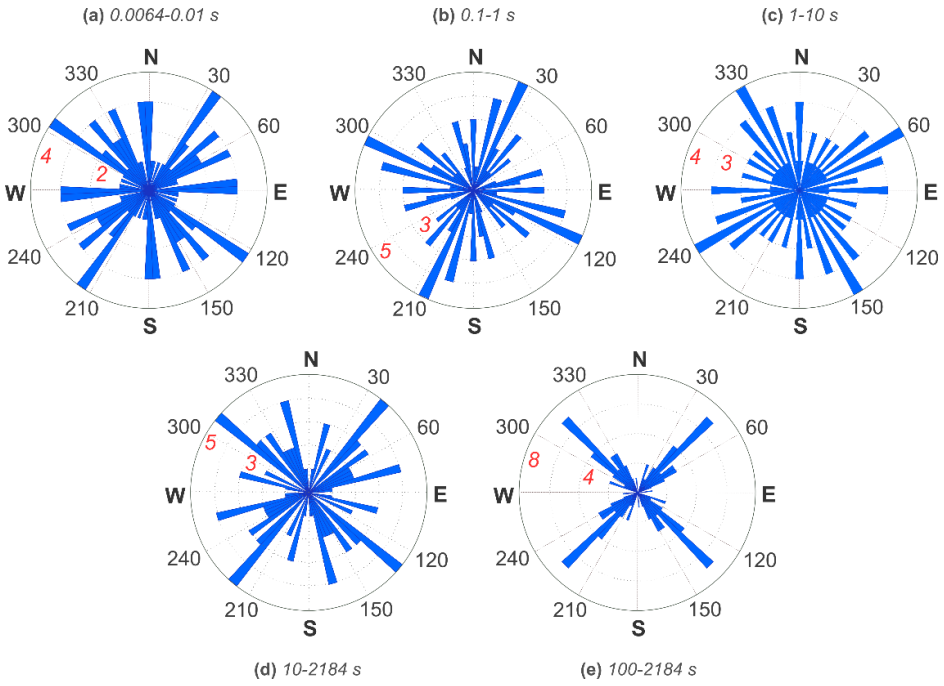

Figure 4: Rose diagrams ranging from 0.0064 to 2184 s (a-e) delineating geoelectric strike directions of the dataset for each station at different depths (periods). The number of sites aligned in a particular orientation is indicated by the inner (red) numbers.

Dimensionality

Dimensionality of the resistivity structure is represented by the shape of the phase tensor ellipse. A circular phase tensor indicates 1D resistivity structure whereas an elliptical phase tensor indicates 2D or 3D structure. Therefore, in order to distinguish between 2D and 3D effects the skew angle (β) was calculated and analysed for each station for periods up to 2184 s.

Skew Angle

A phase tensor pseudosection coloured by the skew angle (β) for periods 0.0064 to 2184 s is shown in Figure 5. Throughout the dataset a series of period bands exhibit high skew values ($\beta > 3°$ or $\beta < -3°$) (i.e. 3D conductivity structure) and hence can be divided into 4 distinct zones. Zone 1 (10^{-2} – 10^{-1} s) represents mostly 2D conductivity structure as demonstrated by the non-circular ellipses and low skew values, with the exception of sites GRA02-GRA05 in the west which exhibit 1D conductivity structure (circular ellipses). Zones 2 (10^{-1} – 10^{0} s) and 3 (10^{0} – 10^{2} s)

predominately exhibit 2-dimensionality. The conductivity structure proceeds to greater complexity with depth and unequivocally 3-dimensional in nature for periods greater than 100 s (Zone 4).

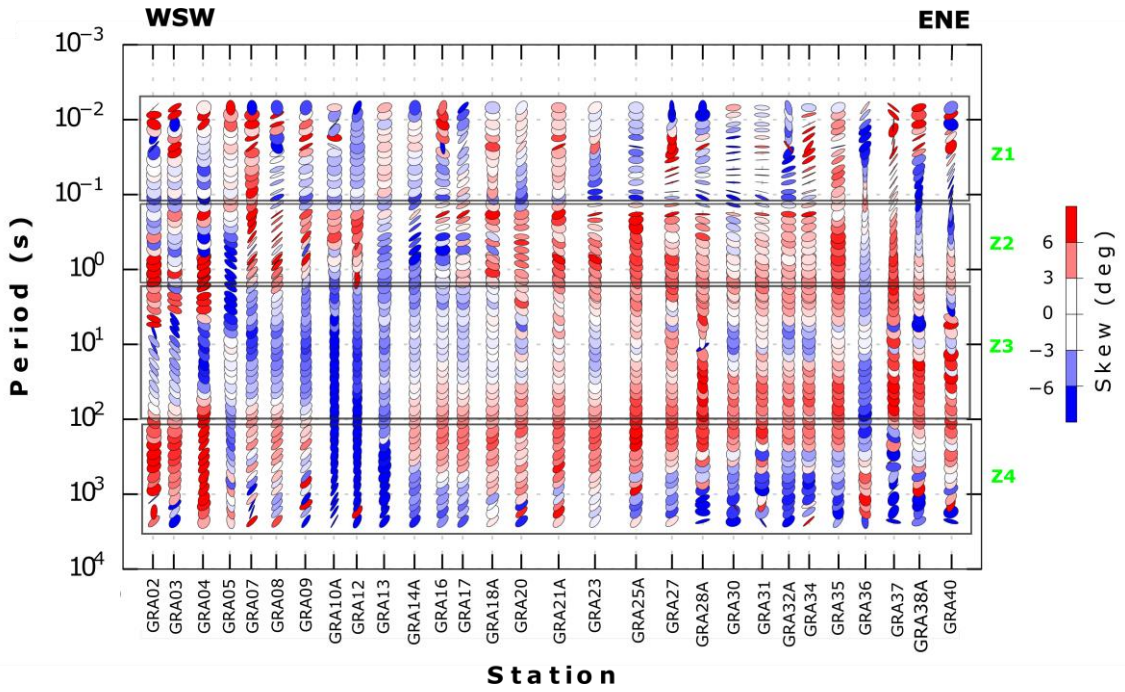

Figure 5: Phase tensor pseudosection plot coloured by skew angle. 3D conductivity structure is inferred if skew angle (β) is > 3° or < −3° (red or blue). The major axis of the ellipse at long periods is aligned in a NE-SW direction which implies a possible geoelectric strike direction (with 90° ambiguity). The dataset can be divided into 4 zones (Z1-Z4).

Minimum Phase Angle

The ellipses were shaded according to the minimum phase angle (Caldwell et al., 2004) and indicate the change of resistivity with depth. Phase tensor ellipses are shown for the observed data, superimposed on regional total magnetic intensity (TMI) and Bouger Gravity images for periods of 0.01, 1, 10, 100 and 1000 s (Figure 6). The survey region can be divided into 4 distinct electrical regions on the basis of changing ellipsoids. Region 1 in the west, is distinguished by high phase angles and circular ellipses at short periods (0.01 s) tending towards more elongate northwest oriented ellipses at intermediate periods (10-100 s). Region 2 is characterised by low phase angles and narrow northeast oriented ellipses at all period ranges.

Comprising the remaining eastern two-thirds of the Grampians-Stavely Zone, Region 3 is characterised by higher minimum phase angles supported by a change in ellipse orientation to approximately N-S to NNE-SSW for periods greater than 1 s.

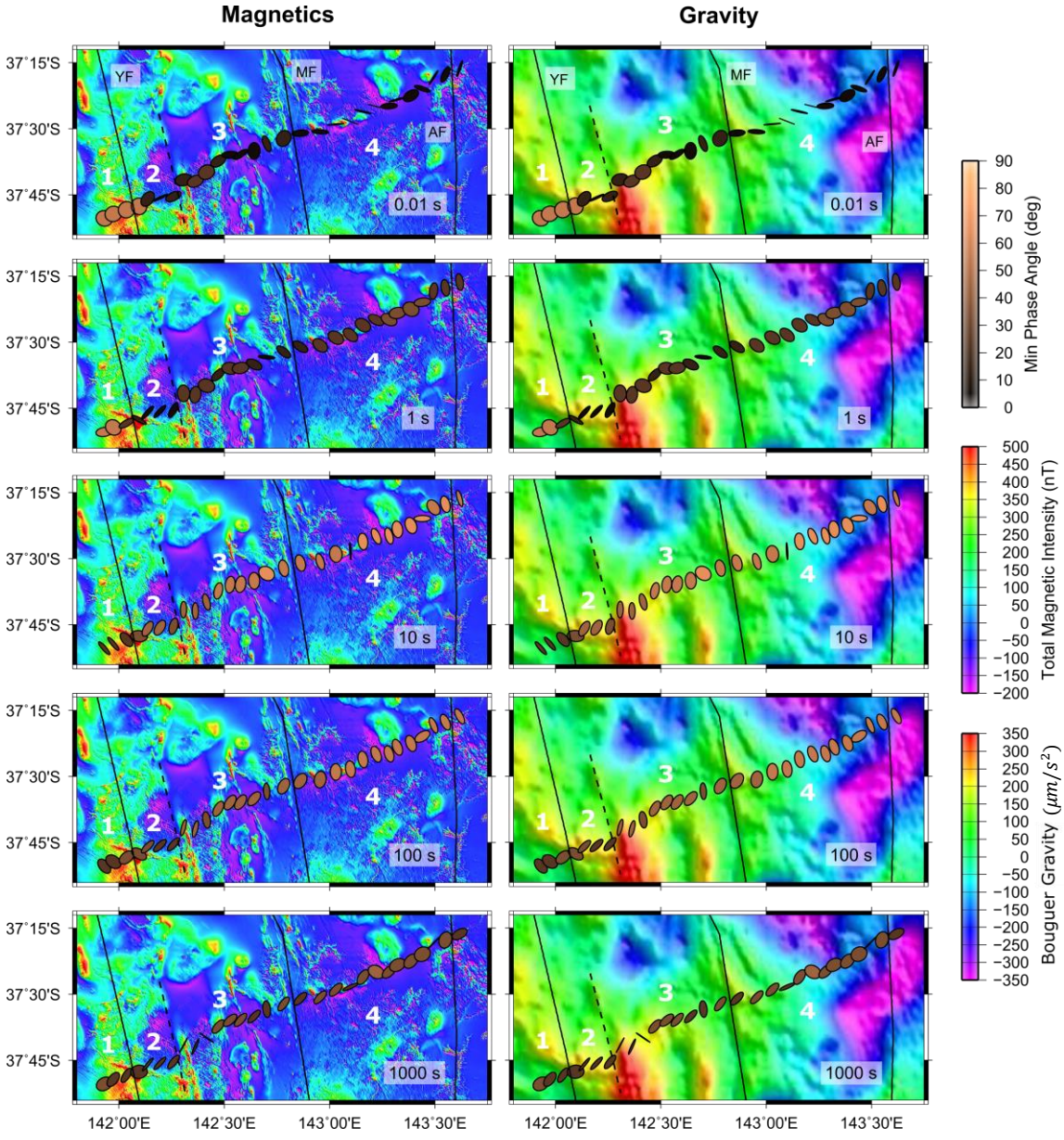

Figure 6: Phase tensor ellipses for each station plotted along profile on top of regional Total Magnetic Intensity (TMI) and Bouguer Gravity maps. Ellipses plotted at periods of 0.01 s, 1 s, 10 s, 100 s and 1000 s. Shading represents minimum phase angle, with values less than 45° representing resistivity increasing with depth and greater than 45° indicating resistivity decreasing with depth. Orientation of ellipses indicates direction of current flow. There are 4 distinct phase tensor gradients (electrical zones) numbered in white, corresponding to the Yarramyljup (YF), Moyston (MF) and Avoca (AF) Faults.

Region 4 is defined by a noticeable change in ellipse orientation at 100 s, rotating to approximately N-S. In addition, higher minimum phase angles at periods of 1, 10 and 100 s are evident, indicating resistivity decreases with depth below this region. No electrical zones were defined east of the Avoca Fault due to inadequate number of acquired sites.

Apparent Resistivity and Phase Pseudosection

The impedance tensor elements (i.e. data) were rotated to align to a geoelectric strike of 45-degrees west of geographic north (N45^{o}W) prior to 2D inversion. This rotation decoupled the MT impedances into two independent modes, with the electric field parallel to the strike for the TE mode (Z_{xy}) and the magnetic field parallel to the strike for the TM mode (Z_{yx}) (Simpson & Bahr, 2005).

The TM mode is more sensitive to lateral resistivity changes, and less influenced by 3D effects compared to the TE mode (Chave & Jones, 2012). The TE mode is heavily influenced by along-strike conductors, whereas the TM mode is most sensitive to resistors and shallow structures. Analysis of the pseudosection highlights general trends of the dataset (Figure 7a-d).

In the west (sites GRA02-GRA05) resistivity decreases at shallow depths (i.e. short periods) indicated by large phase angle (> 45^{o}) (Figure 7b). We also observe a thinning of sediments towards NNE across the length of the upper profile. At longer periods (i.e. greater depths) a trend is observed where resistivity decreases systematically from west to east as indicated by an increase in phase angle (> 45^{o}) (Figure 7d). Changes in conductivity across a boundary generate discontinuous electric fields in the direction perpendicular to the boundary, as a consequence of conservation of current (Simpson & Bahr, 2005). We observe abrupt phase changes in the TM mode indicating conductivity gradients/boundaries (Figure 7c).

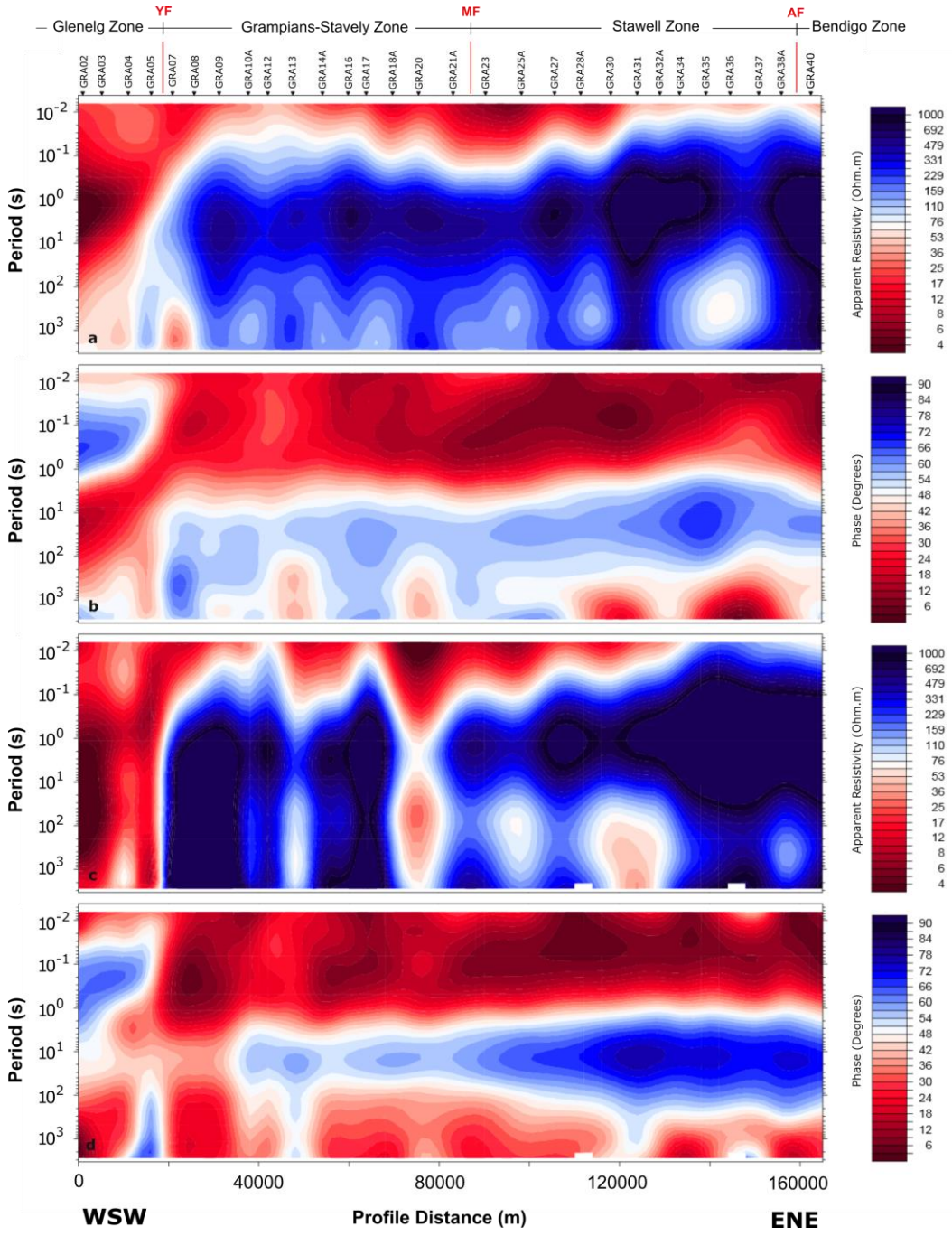

Figure 7: Pseudosection plots of Apparent Resistivity (Ωm) and Phase (degrees) for stations GRA02 to GRA40 representing different polarisation modes; transverse electric (TE) and transverse magnetic (TM). **a.** TE mode: Apparent Resistivity and **b.** Phase **c.** TM mode: Apparent Resistivity and **d.** Phase. The location of the Yarramyljup (YF), Moyston (MF) and Avoca (AF) Faults are shown (red arrows).

MODELLING

2D MT Inversion

2D modelling and inversion of the southwest Victoria transect was carried out within WinGLink software using the 2D inversion algorithm of Rodi and Mackie (2001) for both the TE and TM polarisation modes. Dimensionality analysis revealed the data exhibit predominately 2D to moderate 3D character (skew values greater than 6-degrees). Therefore, 2D modelling was deemed adequate and the preferred option given the data was along a single transect. In addition, it is computationally less expensive compared to 3D modelling given the project time constraints.

A total of 29 stations and 61 periods (0.0064 s - 2184 s) were used for the inversion. Topographic effects were incorporated into the inversion models due to substantial elevation differences (410 m) observed between sites. A starting uniform resistivity of 100 Ωm was used across the model as the base resistivity for all 2D inversions. A uniform grid Laplacian was used for the regularization operator of the WinGLink 2D program.

Phase values are unaffected by galvanic distortion, thus, a higher weighting was specified with respective error floors of 5% for both TE and TM phases for all 2D inversions (Caldwell et al., 2004). The error floor of apparent resistivity for TE and TM modes was set to 10% for all inversions. Flexibility was added during the inversion process enabling the code to automatically adjust for any static shift effects, further enhanced by incorporating a very fine mesh near the surface. Static shift arises from distortion of the electromagnetic field by shallow resistivity anomalies or nearby topography and is a typical problem of the MT method (Árnason, 2008).

Smoothness Parameter (τ)

The aim of MT inversion modelling is to find a model with minimal structure (minimal roughness) while fitting the data with minimal misfit and correlating to geological models (deGroot-Hedlin & Constable, 1990).

For the Rodi and Mackie (2001) algorithm, the smoothness parameter (tau or τ) is a trade-off between the minimum misfit and the smoothest model (Figure 8). Inversion results vary significantly by changes in this parameter, where large values of τ return much smoother models but larger RMS (root mean square) misfit values. Conversely, small values of τ fit the data really well (small RMS misfit) but increase the model roughness by introducing additional structures to the model. Hence, although models with a small τ value are mathematically correct (exceptional fit to the data) they generally do not reflect the level of geological complexity that is sought after and one which is interpretable.

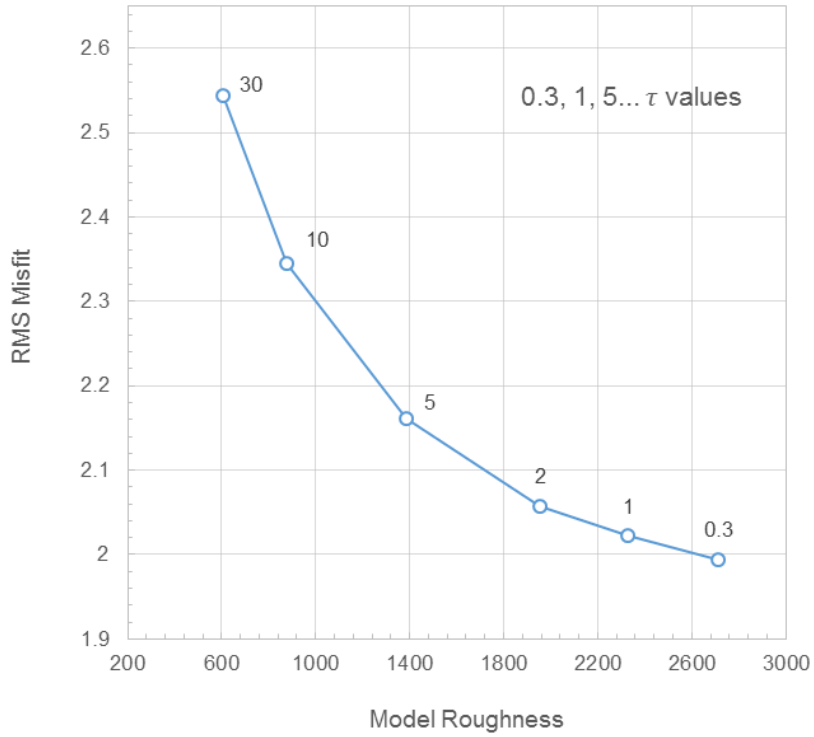

Figure 8: L-curve diagram for the southwest Victoria Transect - RMS Misfit plotted against Model Roughness. Inversions were carried out with different values of the smoothness parameter τ (numbers above the dots). The corner point represents the best compromise between data fit and model smoothness (Hansen, 1998). A value of τ = 5 was found and hence, used for all subsequent inversions.

A standard procedure for estimating the optimal τ value was carried out - known as the L-curve study (see Hansen, 1998; Muñoz, Ritter, & Moeck, 2010). A number of inversions were run with differing τ values, where each models RMS misfit was plotted against model roughness. The optimal value for τ was found close to the

corner point of the L-curve where minimisation of both terms (maximum curvature) occurs, corresponding to a smoothing parameter of τ = 5 (Figure 8).

Weighted Smoothing (α, β)

Two additional smoothing factors, alpha (α) and beta (β) were applied to the model and their overall influence measured. Beta controls the relative smoothness of deeper and shallower regions of the model whereas alpha weights horizontal smoothness over vertical smoothness. Beta has a greater effect on the model compared to alpha, as exponential and multiplicative factors, respectively. Multiple inversions were run with a tau value of 5 with model outputs analysed in terms of their best fit to the data (i.e. lowest RMS error). A final model with smoothing parameters (α, β) set at 1 represented the best fit to the data, with a final RMS of 2.26 and model roughness of 1089 obtained (Figure 9).

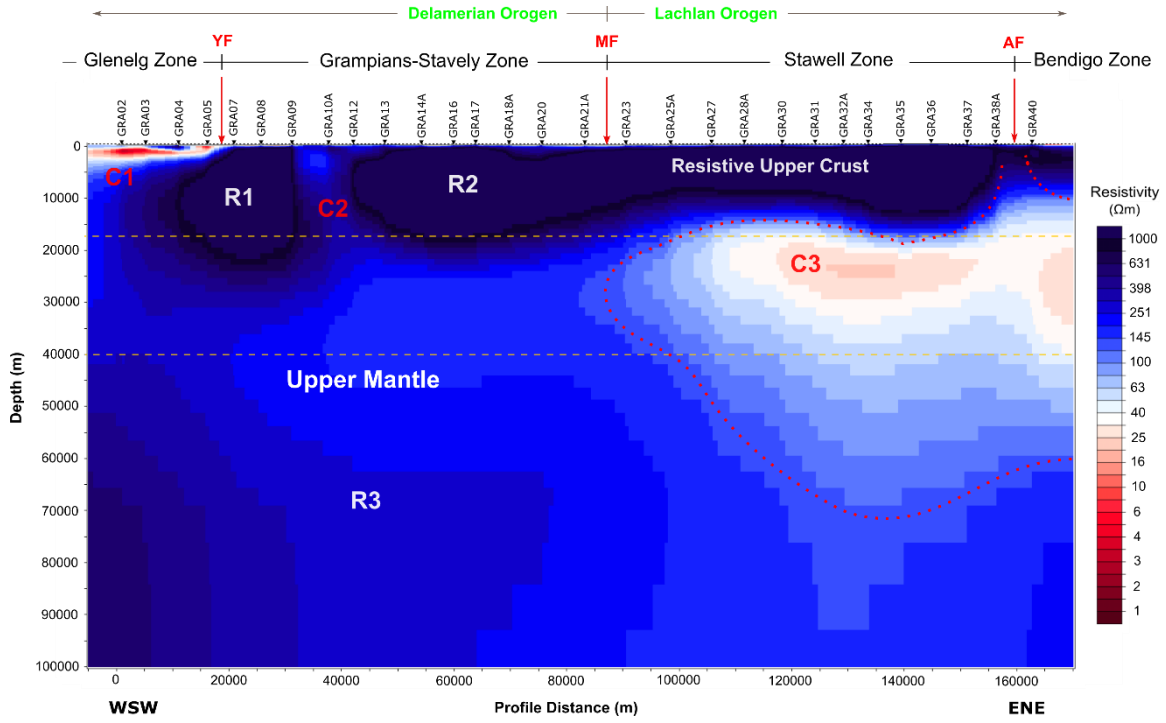

Figure 9: WinGLink 2D model from inversion of all data from 29 stations (GRA02 to GRA40) of the southwest Victoria Transect. Modelling of both the transverse electric and transverse magnetic modes. Blue regions are resistive (R1, R2, R3), red are conductive (C1, C2, C3). Red dotted outline represents conductive crust of the Lachlan Orogen. Yellow horizontal dashed lines mark the transition between the upper crust, lower crust and upper mantle (approximately). The location of the Yarramyljup (YF), Moyston (MF) and Avoca (AF) Faults are shown (red arrows).

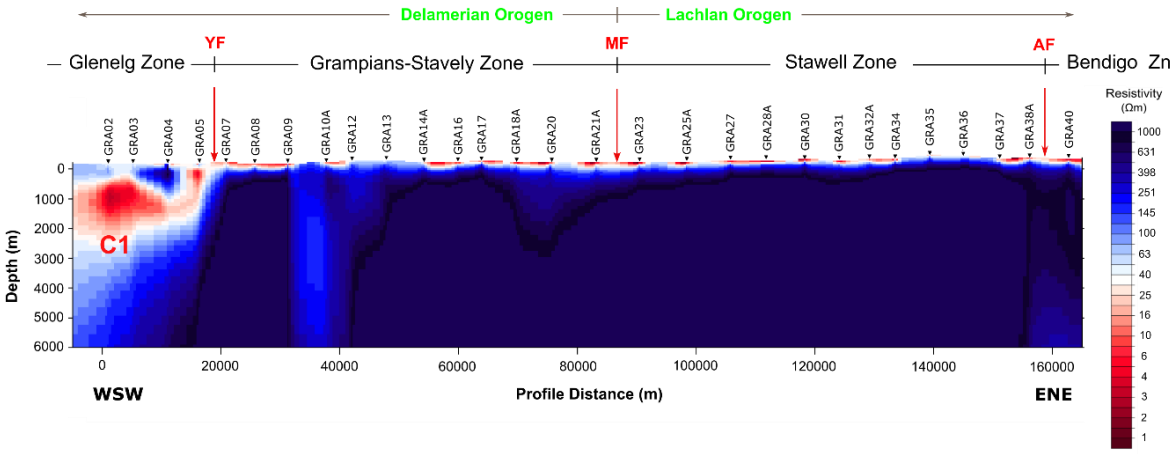

Figure 10: WinGLink 2D inversion model zoomed in to the top 6 km imaging the sediments (regolith) and basins of the upper crust. A vertical (depth) exaggeration (5:1) has been applied for visualisation purposes. Red regions are conductive, blue are resistive. Highly conductive (1-15 Ωm) sediments observed across the upper 200-300 m of the profile, thinning towards ENE. A ~3km thick conductive region (C1) in the west represents a dense sequence of Otway Basin sediments.

Observed Anomalies

A 1-10 Ωm shallow conductivity anomaly (C1) was detected south of Hamilton at 1 to 2.5 km depth (sites GRA02-GRA05; Figures 9, 10). The lower crust and upper mantle of the entire western region of the model (R3) shows moderate-high resistivity (200-800 Ωm). The eastern half of the model contains more striking features in particular a large conductivity anomaly (C3) with resistivity values ranging from 10-30 Ωm. The conductor is situated predominately within the lower crust approximately 12-15 km below the surface, extending into the upper mantle (40-50 km depth). The eastern tip of this C3 conductor migrates to a depth of ~ 5 km below the surface (Figure 9).

The model shows upper crustal heterogeneity with two large resistive bodies (> 1000 Ωm) extending from the near-surface to a thickness ranging from 10-20 km (R1 and R2) (Figure 9). The two bodies are separated by a drop in resistivity signified by an east dipping moderate conductor (C2) (100-150 Ωm).

WinGLink Modelled Response Curves

The inversion of MT data in WinGLink produced model response curves for each station showing a statistical measure of how closely the data fits the model - known as the RMS misfit (see Appendix C).

Sensitivity Analysis

To determine whether the modelled features were real, a sensitivity analysis was carried out on the 2D inversion model by changing the base resistivity values of the starting model. Resistivity values (10-10,000 Ωm) were applied and the output models compared to determine how robust the modelled features were. In addition, an inversion of only the TM mode was also conducted. Both sensitivity analyses returned consistent results with the models successfully imaging the features obtained in the final model. The robustness of the model (Figure 9) was therefore confirmed with no significant artefacts present.

Integration with Seismic Data

MT models ascertain greater value when combined with multi-disciplinary geophysical measurements such as seismic and gravity (e.g. Nagy, 1996; Robertson, Taylor, Thiel, & Heinson, 2015). Seismic lines 06GA-V1 and 09GA-AR1 have been overlain on corresponding sections of the 2D model covering the eastern and middle regions of the profile, respectively (Figures 11, 12). Strong correlation between major lithological units and electrical structure is observed (Figure 11). In addition, regions of low seismic reflectivity correlate to higher conductivities within the upper and lower crust (Figure 12).

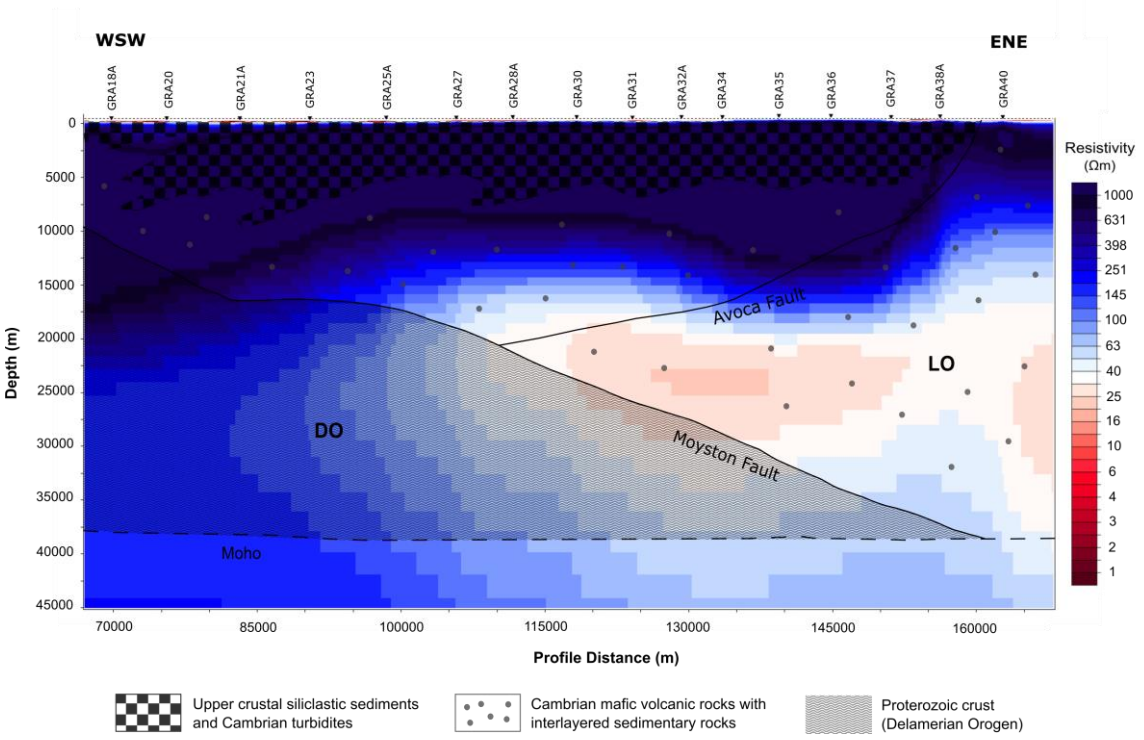

Figure 11: Interpreted seismic reflection profile from seismic line 06GA-V1 (modified from Cayley, Korsch, Moore, et al., 2011) overlain on MT data (stations GRA18A-GRA40). The distribution of first order faults and major lithological units (see legend) between the surface and the Moho (dashed-line) (TWT ~14 s) is shown. Black solid lines represent major faults. Good correlation between lithology and electrical structure is observed. Upper crustal (highly resistive), mid-crustal (conductive) and lower (western) crustal (moderately resistive). LO = Lachlan Orogen, DO = Delamerian Orogen.

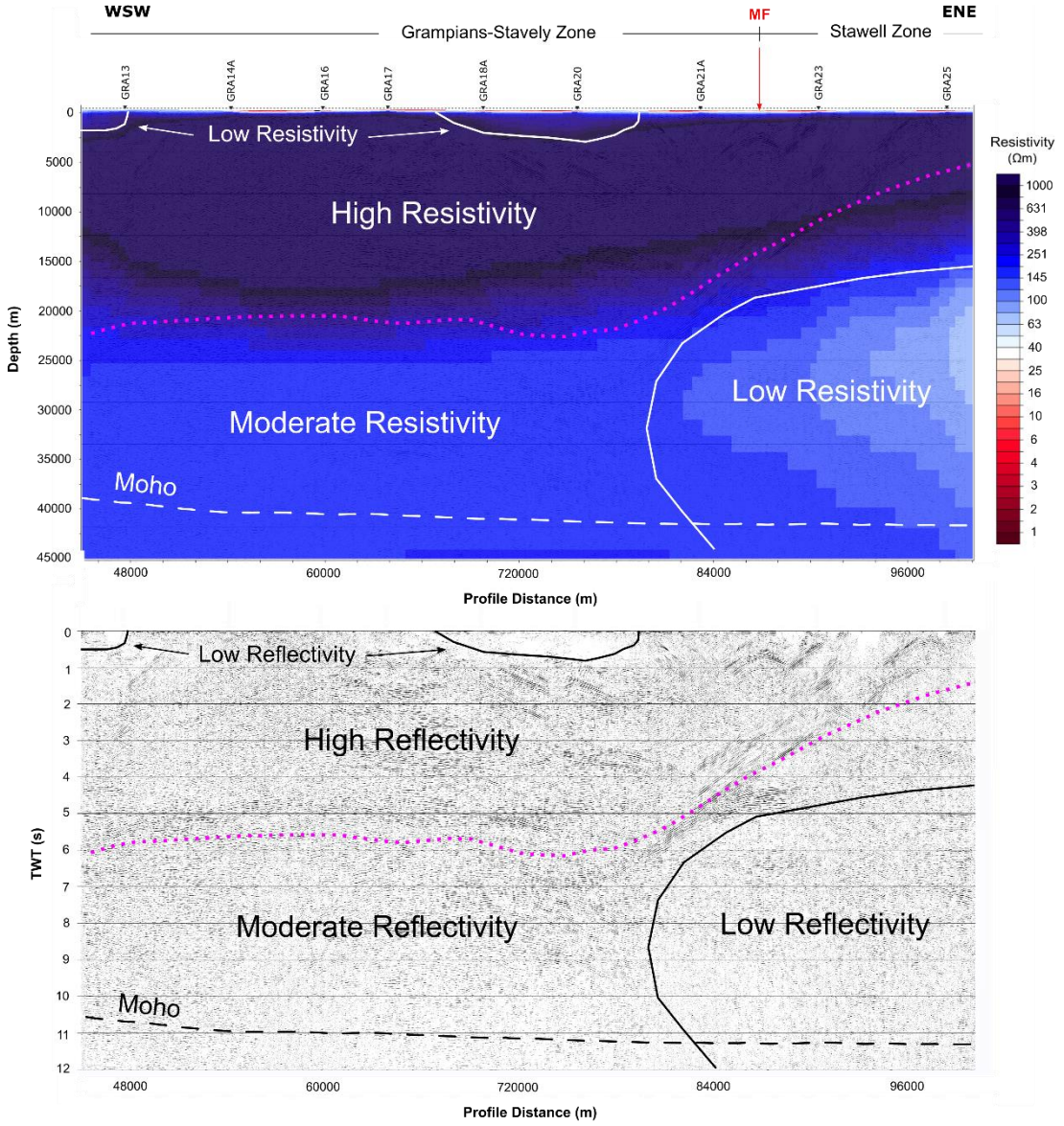

Figure 12: Seismic reflection profile (raw migrated data) from seismic line 09GA-AR1 (bottom) overlain on MT data (stations GRA13-GRA25) (top). Zones of low reflectivity compared with zones of low resistivity show correlation, and vice versa. Solid lines (black/white) represent zones of low reflectivity or low resistivity. Purple dotted line separates zones of high reflectively and resistivity to zones of moderate reflectively and resistivity.

AusLAMP Victoria 3D Comparison

Comparison of the southwest Victoria 2D model to the AusLAMP Victorian 3D model at 39 km depth (lower crust) reveal a matching systematic decrease in resistivity from west-east (Figure 13). The 2D model shows a lower resistivity (white) bulb extending further westward, however this is inconsistent with the 3D model.

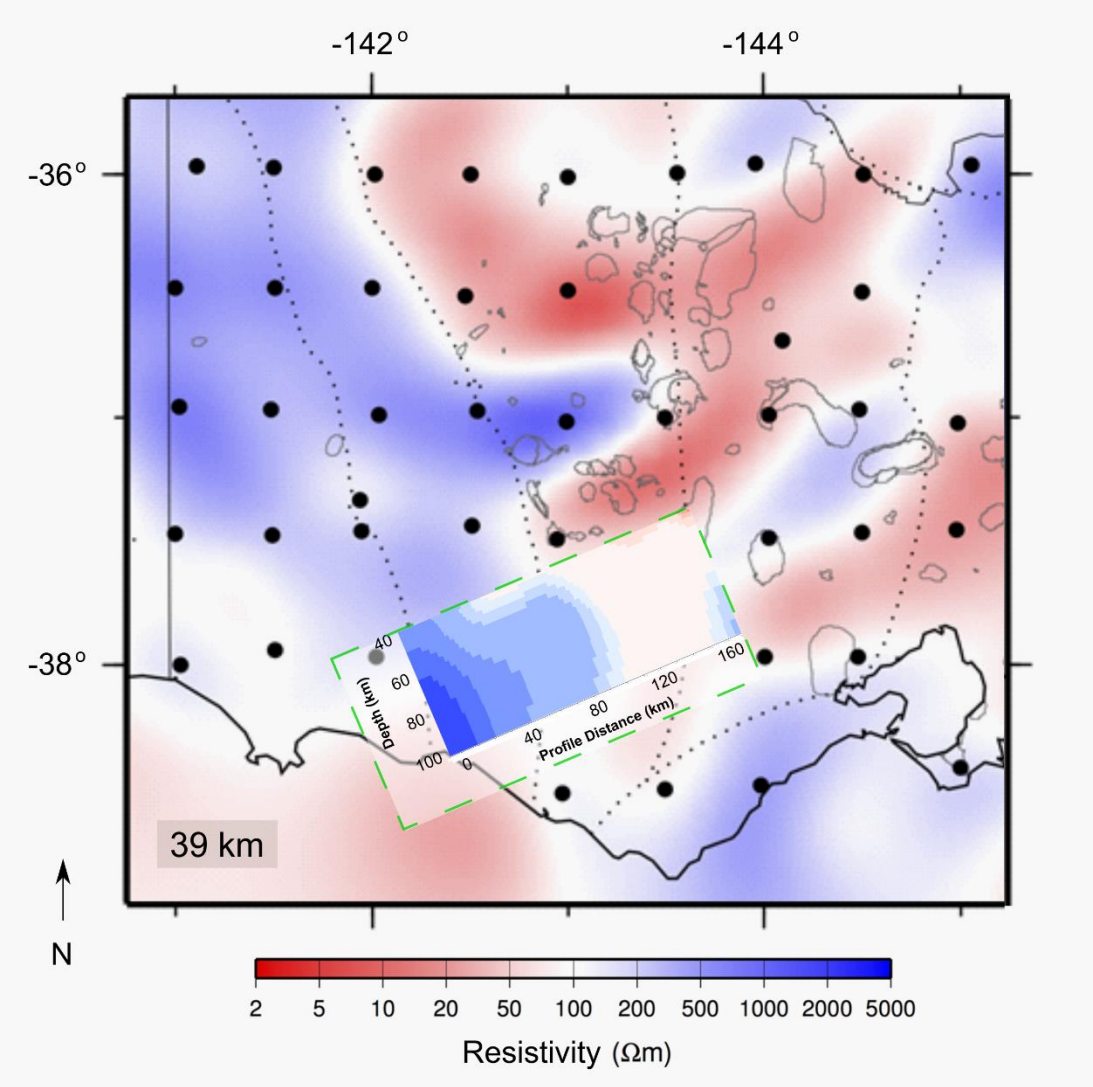

Figure 13: WinGLink 2D inversion model (green-dashed profile; resistivity colour scale equivalent) overlaying AusLAMP Victoria 3D model depth slice at 39 km (base of the crust). Good correlation between models is observed with the western region more resistive (blue), transitioning to more conductive (red) in the east. Devonian granite intrusions (grey outlines). AusLAMP acquisition sites (black dots). Modified after Duan et al., (2016).

DISCUSSION

The continuation of a relict west-dipping conductive anomaly representative of a Cambrian subduction system as suggested by Robertson, Taylor, Thiel, et al. (2015) was not imaged below the western Stawell Zone in our 2D modelling as the geology would suggest. Nevertheless, anomalies within the crust and upper mantle plus a distinct resistivity gradient from west to east were resolved, and are discussed below.

Geological Explanation of Resistivity Anomalies

Upper Crust

The uppermost horizontal conductivity layer (1-25 Ωm) imaged within top 300 m of the surface can be attributed to sedimentary basins and regolith cover comprising of relatively young, unconsolidated sediments with high porosities and permeabilities (Figure 10; Freeze & Cherry, 1979). Conductive anomaly C1 in the west just south of Hamilton may be representative of the Otway Basin covering on and offshore southwestern Victoria. As shown by Kirkby, Heinson, Holford, and Thiel (2015) the sediments of Otway Basin are isotropic and highly conductive (1-10 Ωm) within the upper 3 km. This is comparative to our model where the anomaly extends from ~0.5-2.5 km depth with conductivities ranging from 1-10 Ωm. Beyond 3 km depth conductivity decreases systematically. This is likely due to the relative thickness of these sediments, with this region likely to have attenuated signal, thereby decreasing the resolution (skin depth) and inhibiting the modelled electrical structure of the lower crust and upper mantle.

The Lachlan Orogen represents a turbidite dominated accretionary orogen whereby continental growth occurred through the accretion of large turbidite fans underlain by a tectonically imbricated layer of oceanic crust, generating a two-tiered accreted crust (Foster & Goscombe, 2013). Hence, the high resistivity (> 1000 Ωm) of the mid-upper crust (R2) below the Stawell and Bendigo Zones is representative of Cambrian turbidite sequences metamorphosed under greenschist conditions, exhibiting low porosities and permeabilities (Cayley, Korsch, Moore, et al., 2011; Foster &

Goscombe, 2013). The narrow C2 mid-upper crustal conductor (150-300 Ωm) is distinct from rest of the profile and may represent a fossil fluid pathway emanating from the lower crust/upper mantle (Figure 9). This conductive anomaly is also observed in more northern 2D transects indicating the feature is continuous N-S (see Robertson, Taylor, Thiel, et al., 2015).

Lower Crust and Upper Mantle

The broad C3 conductive anomaly (10-30 Ωm) in the east of the profile resides predominately within the lower crust and upper mantle, below the Bendigo and Stawell Zones (Figure 9). Measured isotopic compositions and trace-elements of whole-rocks and metasomatic phases from west Victorian xenoliths record multiple discrete episodes of modal metasomatism by at least two different types of fluid, one silicate rich and one carbonatitic rich (Powell, Zhang, O'Reilly, & Tiepolo, 2004). The observed silicate metasomatism may be related to a 300-500 Ma event in which basaltic melts crystallised in the lithospheric mantle (Powell et al., 2004). This observed anomaly also aligns with the 3D Victorian AusLAMP model where a conductive mantle (50 Ωm) merges vertically upwards into a series of northeast-southwest trending conductive anomalies within the mid- lower crust (Figure 13; Duan et al., 2016). The lower crustal conductor observed in both models is spatially consistent with the distribution of near-surface Devonian Granite intrusions (Figure 13). Therefore, we infer the anomaly to mark a fossil metasomatised ascent path of granitic melts rising through the lower crust, overprinting the dominant north-south structural trend of the hosting bedrock. The lower crustal lithology accommodating the anomaly inferred from deep seismic profiling suggests a mix of sedimentary and Cambrian mafic volcanic rocks and Proterozoic crust of the Delamerian Orogen across the Moyston Fault (Figure 11; Cayley, Korsch, Moore, et al., 2011)

Effects of such fluid alteration (metasomatism) may be apparent in the Ararat to Hamilton seismic line (09GA-AR1) adjacent to the MT transect, where a correlation between low reflectivity and low resistivity is observed (Figure 12). Global deep seismic reflection profiling reveals the middle and lower continental crust is usually

reflective (Klemperer, 1987). The Ararat to Hamilton seismic data indicates a reflective upper and middle crust but a non-reflective lower crust (Figure 12). The low reflectivity may be attributed to broad-scale fluid alteration, enhancing the conductivity of the host rocks and resetting any acoustic impedance variation that would give rise to reflection. Two additional non-reflective features identified within the top 3 km of the same profile (Figure 12) are interpreted as Cambrian pelitic (clay-rich) metasedimentary rocks (Cayley, Korsch, Kennett, et al., 2011) giving rise to their moderate conductivity (150 Ωm; Simpson & Bahr, 2005).

The product of an enriched lithosphere (hydrogen) may also be evident within the model, arising from the processes of Cambrian subduction persisting over geological time scales (Figure 9; Demouchy, 2010; Plank & Langmuir, 1998; Sleep, 2009). However, this increased resistivity signature is presumed to have been overprinted and further enhanced by metasomatic processes throughout the crust and upper mantle (post-subduction), as discussed above.

Delamerian and Lachlan Orogen Transition

The most distinctive feature identified from the 2D model is the major west to east trend in electrical resistivity of the lower crust and upper mantle, representative of the transition zone between the Delamerian and Lachlan Orogens (Figure 9). The Stawell and Bendigo Zones (Lachlan Orogen) are more conductive than their Delamerian counterparts (Glenelg and Grampians-Stavely Zones). This abrupt transition is coincident with the location of the Mortlake Discontinuity which represents a distinguishable change in strontium (Sr) and lead (Pb) isotope ratios of the Newer Volcanic Province basalts (Price et al., 1997). The Delamerian Orogen is depleted in Sr relative to the Lachlan Orogen with a lower mean $^{87}Sr/^{86}Sr$ ratio - 0.7042 compared to 0.7047 (Price et al., 1997). Variation across this boundary is either due to crustal contamination of the magma during ascent or a differing mantle source. The electrical resistivity gradient occurs down to periods of at least 1000 s (upper mantle depths) as identified by phase tensor ellipses (Figure 6) and 2D inversion modelling (Figure 9). In addition, a large velocity difference is observed

across this boundary to depths greater than 200 km (Rawlinson, Salmon, & Kennett, 2014). This suggests the Mortlake Discontinuity is representative of upper mantle depths, supportive of the differing mantle source hypothesis.

Comparison with Crustal Seismic Velocities and Gravity

A seismic tomography study by Jiang et al. (2016) shows high mid-crustal (10-15 km) velocities dominate regions west of the Moyston Fault (Delamerian Orogen), separated by low velocities to the east (Lachlan Orogen). However, at these depths a change in resistivity is not yet observed in our model, only when depths exceed 20 km. Furthermore, the seismic velocity trends at greater crustal depths (30 km) become more complex and do not correlate well with resistivity.

This crustal seismic velocity variation throughout the crust may be attributed to the presence of buried magmatic arcs (Jiang et al., 2016) and/or a reworked orogenic zone (Miller et al., 2005) blurring the transition between the Delamerian and Lachlan Orogens. However, seismic velocity gradients are more distinct at mantle depths, with faster velocities observed west of the Moyston Fault in addition to a positive Bouguer Gravity anomaly above the Delamerian Orogen (Figure 6). This may represent the vastly different lithospheric architecture (composition and age) of the two Orogens. The Delamerian Orogen is presumed to be Precambrian lithosphere of continental origin, compared to thinner Palaeozoic Lachlan Orogen lithosphere that is purely oceanic (Foster & Gray, 2000; Spaggiari, Gray, Foster, & McKnight, 2003) or mixed oceanic-continental ancestry (Taylor & Cayley, 2000; VandenBerg, 1999; Willman, VandenBerg, & Morand, 2002).

Geological Zones Constrained from Electrical Responses

The geological zones of western Victoria representative of the sub-boundaries of the Delamerian and Lachlan Orogens were previously defined by Robertson, Taylor, Thiel, et al. (2015) through phase tensor ellipse analysis in an MT survey approximately 40 km north of the study region. Our results show the continuation of these geological boundaries further southwards where 4 electrical regions have been characterised (Figure 6).

Region 1 is defined as the Glenelg Zone and is bound by the Yarramyljup fault to the east indicated by a sharp contrast in resistivities between sites GRA05 and GRA07 (Figures 9, 10). The dip of the fault is towards the west, consistent with seismic profiling marking the western limit of exploration interest for the Stavely Copper Porphyries Project. The Grampians-Stavely Zone is representative of Regions 2 and 3, sub-divided by a mid-upper crustal conductor (C2) (Figure 9). Region 3 continues across the remaining two-thirds of the Grampians-Stavely Zone terminating against the Moyston Fault signified by an increase in phase angle, thereby marking the beginning of the Stawell Zone (Region 4). Phase tensor analysis across the inferred Avoca Fault shows no observable change possibly due to the presence of a single site. However, 2D modelling reveals a west dipping resistivity gradient beneath site GRA38A (Figure 9) indicative of the Avoca Fault and thus defining the Bendigo Zone to the east.

This analysis has resulted in more constrained and resolute boundaries across southwestern Victoria having important implications on future mineral exploration in the region given the Glenelg, Grampians-Stavely and Stawell Zones represent the remnant back-arc, arc and fore-arc subduction accretion terranes, respectively (Foden et al., 2006; Kemp, 2003; Miller et al., 2005).

CONCLUSIONS

The electrical resistivity structure of the lithosphere beneath southwestern Victoria has been imaged using magnetotellurics traversing the transition between the Delamerian and Lachlan Orogens. 2D inversion modelling reveals a more conductive lower crust and upper mantle beneath the Lachlan Orogen, compared to the Delamerian Orogen. We attribute the west to east resistivity gradient as the boundary between the two Orogens coinciding with the Moyston Fault and the location of the Mortlake Discontinuity down to depths representative of the upper mantle. A positive gravity anomaly and faster seismic velocities above the Delamerian Orogen supports such a boundary. This correlates to a change in lithospheric composition of the Delamerian Orogen (Precambrian lithosphere of continental origin) and the Lachlan Orogen (Paleozoic lithosphere of purely oceanic or mixed oceanic-continental origin).

Evidence of a metasomatised mantle below southwestern Victoria and a spatial link with Devonian granite intrusions suggests the broad conductive anomaly (C3) below the Stawell and Bendigo Zones represents fossil metasomatised ascent paths of granitic melts within the lower crust and upper mantle. A pre-existing enriched lithosphere from subduction related processes is likely to have been overprinted by this event. As such, continuation of a relict west-dipping subduction zone below the western Stawell Zone was not imaged in this more southward transect. Furthermore, alignment of low seismic reflectivity and low resistivity zones resemble broad-scale alteration, enhancing the conductivity and resetting the reflective signature of the host rocks.

The Glenelg, Grampians-Staveley, Stawell and Bendigo geological zones were successfully defined through phase tensor analysis with continuation of these boundaries further south assisting future mineral exploration in the region. The availability of offline sites including AusLAMP Victoria and parallel transects will enable the application of 3D modelling of this transect in the future to better constrain the resistivity structures below southwest Victoria.

ACKNOWLEDGEMENTS

It is a pleasure to thank the following people who made this thesis possible though their valued contributions. Many thanks to David Taylor for field assistance and providing insights into the geology of Victoria; Kate Robertson for technical expertise on the MT method, assistance with field deployment and providing valued feedback and discussions; Doctor Yohannes Didana for guidance and knowledge on MT data processing and modelling; Alison Kirkby for field assistance and support with Python; Doctor Adam (Luo YaoHua) for assistance in the field and Goran Boren for maintaining the field equipment. I would finally like thank my supervisor Professor Graham Heinson for his superior guidance and providing me the opportunity to work with MT this year. Equipment was supplied by the national provider AuScope, with generous funding provided by the University of Adelaide and the Victorian Geological Survey.

REFERENCES

AIVAZPOURPORGOU, S., THIEL, S., HAYMAN, P. C., MORESI, L. N., & HEINSON, G. (2015). Decompression melting driving intraplate volcanism in Australia: Evidence from magnetotelluric sounding. *Geophysical Research Letters, 42*(2), 346-354.

ÁRNASON, K. (2008). The Magnetotelluric static shift problem. *Iceland GeoSurvey Report ÍSOR/08088, Reykjavik, Iceland*.

BECKEN, M., & BURKHARDT, H. (2004). An ellipticity criterion in magnetotelluric tensor analysis. *Geophysical Journal International, 159*(1), 69-82.

BIBBY, H. M., CALDWELL, T. G., & BROWN, C. (2005). Determinable and non-determinable parameters of galvanic distortion in magnetotellurics. *Geophysical Journal International, 163*(3), 915-930. doi: 10.1111/j.1365-246X.2005.02779.x

BOYCE, J. (2013). The Newer Volcanics Province of southeastern Australia: a new classification scheme and distribution map for eruption centres. *Australian Journal of Earth Sciences, 60*(4), 449-462.

BOYCE, J., NICHOLLS, I., KEAYS, R., & HAYMAN, P. (2014). Victoria erupts: the Newer Volcanics Province of south-eastern Australia. *Geology Today, 30*(3), 105-109.

CALDWELL, T. G., BIBBY, H. M., & BROWN, C. (2004). The magnetotelluric phase tensor. *Geophysical Journal International, 158*(2), 457-469. doi: 10.1111/j.1365-246X.2004.02281.x

CAYLEY, R., KORSCH, J., MOORE, H., COSTELLOE, D., NAKAMURA, A., WILLMAN, E., . . . O'SHEA, J. (2011). Crustal architecture of central Victoria: results from the 2006 deep crustal reflection seismic survey. *Australian Journal of Earth Sciences, 58*(2), 113-156. doi: 10.1080/08120099.2011.543151

CAYLEY, R., KORSCH, R., KENNETT, B., SKLADZIEN, P., JONES, L., MORAND, V., . . . BETTS, P. (2011). Results of deep seismic reflection imaging of the eastern Delamerian Orogen, South Australia and western Victoria, Australia. *Data CD version, 4*.

CAYLEY, R., & TAYLOR, D. (2001). Ararat 1: 100 000 geological map report. *Geological Survey of Victoria Report, 115*.

CAYLEY, R., TAYLOR, D., VANDENBERG, A., & MOORE, D. (2002). Proterozoic–Early Palaeozoic rocks and the Tyennan Orogeny in central Victoria: the Selwyn Block and its tectonic implications. *Australian Journal of Earth Sciences, 49*(2), 225-254.

CHAPPELL, B., WHITE, A., & HINE, R. (1988). Granite provinces and basement terranes in the Lachlan Fold Belt, southeastern Australia. *Australian Journal of Earth Sciences, 35*(4), 505-521.

CHAVE, A., & JONES, A. (2012). *The magnetotelluric method: Theory and practice*: Cambridge University Press.

CHAVE, A., & THOMSON, D. (2004). Bounded influence magnetotelluric response function estimation. *Geophysical Journal International, 157*(3), 988-1006. doi: 10.1111/j.1365-246X.2004.02203.x

DEGROOT-HEDLIN, C., & CONSTABLE, S. (1990). Occam's inversion to generate smooth, two-dimensional models from magnetotelluric data. *GEOPHYSICS, 55*(12), 1613-1624. doi: 10.1190/1.1442813

DEMOUCHY, S. (2010). Hydrogen diffusion in spinel grain boundaries and consequences for chemical homogenization in hydrous peridotite. *Contributions to Mineralogy and Petrology, 160*(6), 887-898.

DIREEN, N., & CRAWFORD, A. (2003). The Tasman Line: where is it, what is it, and is it Australia's Rodinian breakup boundary? *Australian Journal of Earth Sciences, 50*(4), 491-502.

DUAN, J., TAYLOR, D., CZARNOTA, K., CAYLEY, R., & CHOPPING, R. (2016). AusLAMP MT Over Victoria: New Insight from 3D Modelling Highlights Regions of Anomalously Conductive Mantle and Unexpected Linear Trends in the Crust. *ASEG Extended Abstracts, 2016*(1), 1-6.

EVERETT, M. E. (2005). What do electromagnetic induction responses measure? *The Leading Edge, 24*(2), 154-157.

FODEN, J., ELBURG, M., DOUGHERTY-PAGE, J., & BURTT, A. (2006). The Timing and Duration of the Delamerian Orogeny: Correlation with the Ross Orogen and Implications for Gondwana Assembly. *The Journal of Geology, 114*(2), 189-210. doi: 10.1086/499570

FOSTER, D., & GOSCOMBE, B. (2013). Continental growth and recycling in convergent orogens with large turbidite fans on oceanic crust. *Geosciences, 3*(3), 354-388.

FOSTER, D., & GRAY, D. (2000). Evolution and Structure of the Lachlan Fold Belt (Orogen) of Eastern Australia. *Annual Review of Earth and Planetary Sciences, 28*(1), 47-80. doi: 10.1146/annurev.earth.28.1.47

FOWLER, C. M. R. (2012). The Earth: Core, mantle and crust. In A. Bally (Ed.), *Regional Geology and Tectonics: Principles of Geologic Analysis* (pp. 18-39). Amsterdam: Elsevier.

FREEZE, R. A., & CHERRY, J. A. (1979). *Groundwater*. Englewood Cliffs: Prentice-Hall.

GAINA, C., MÜLLER, D. R., ROYER, J. Y., STOCK, J., HARDEBECK, J., & SYMONDS, P. (1998). The tectonic history of the Tasman Sea: a puzzle with 13 pieces. *Journal of Geophysical Research: Solid Earth, 103*(B6), 12413-12433.

GAMBLE, T. D., GOUBAU, W. M., & CLARKE, J. (1979). Error analysis for remote reference magnetotellurics. *GEOPHYSICS, 44*(5), 959-968. doi: 10.1190/1.1440988

GLEN, R. (2005). The Tasmanides of eastern Australia. *Geological Society, London, Special Publications, 246*(1), 23-96.

GLEN, R. (2013). Refining accretionary orogen models for the Tasmanides of eastern Australia. *Australian Journal of Earth Sciences, 60*(3), 315-370.

GLEN, R., SCHEIBNER, E., & VANDENBERG, A. (1992). Paleozoic intraplate escape tectonics in Gondwanaland and major strike-slip duplication in the Lachlan orogen of southeastern Australia. *Geology, 20*(9), 795-798.

GRAY, D., & FOSTER, D. (2004). Tectonic evolution of the Lachlan Orogen, southeast Australia: historical review, data synthesis and modern perspectives. *Australian Journal of Earth Sciences, 51*(6), 773-817.

GROOM, R. W., & BAILEY, R. C. (1989). Decomposition of magnetotelluric impedance tensors in the presence of local three-dimensional galvanic distortion. *Journal of Geophysical Research: Solid Earth, 94*(B2), 1913-1925.

HANSEN, P. C. (1998). *Rank-deficient and discrete ill-posed problems: numerical aspects of linear inversion* (Vol. 4): Siam.

JIANG, C., YANG, Y., RAWLINSON, N., & GRIFFIN, W. L. (2016). Crustal structure of the Newer Volcanics Province, SE Australia, from ambient noise tomography. *Tectonophysics, 683*, 382-392.

JONES, A. G. (1999). Imaging the continental upper mantle using electromagnetic methods. *Lithos, 48*(1), 57-80.

KEMP, A. (2003). Plutonic boninite-like rocks in an anatectic setting: Tectonic implications for the Delamerian orogen in southeastern Australia. *Geology, 31*(4), 371-374.

KEMP, A., HAWKESWORTH, C., COLLINS, W., GRAY, C., & BLEVIN, P. (2009). Isotopic evidence for rapid continental growth in an extensional accretionary orogen: The Tasmanides, eastern Australia. *Earth and Planetary Science Letters, 284*(3), 455-466.

KIRKBY, A., HEINSON, G., HOLFORD, S., & THIEL, S. (2015). Mapping fractures using 1D anisotropic modelling of magnetotelluric data: A case study from the Otway Basin, Victoria, Australia. *Geophysical Journal International, 201*(3), 1961-1976.

KLEMPERER, S. L. (1987). A relation between continental heat flow and the seismic reflectivity of the lower crust. *Geophysical Journal International, 61*(1), 1-11.

LEDO, J., JONES, A. G., SINISCALCHI, A., CAMPANYÀ, J., KIYAN, D., ROMANO, G., . . . TEAM, T. M. (2011). Electrical signature of modern and ancient tectonic processes in the crust of the Atlas mountains of Morocco. *Physics of the Earth and Planetary Interiors, 185*(3), 82-88.

LESTI, C., GIORDANO, G., SALVINI, F., & CAS, R. (2008). Volcano tectonic setting of the intraplate, Pliocene-Holocene, Newer Volcanic Province (southeast Australia): Role of crustal fracture zones. *Journal of Geophysical Research: Solid Earth, 113*(B7).

MILLER, J. M., PHILLIPS, D., WILSON, C., & DUGDALE, L. (2005). Evolution of a reworked orogenic zone: The boundary between the delamerian and lachlan fold belts, southeastern Australia. *Australian Journal of Earth Sciences, 52*(6), 921-940.

MUÑOZ, G., RITTER, O., & MOECK, I. (2010). A target-oriented magnetotelluric inversion approach for characterizing the low enthalpy Groß Schönebeck geothermal reservoir. *Geophysical Journal International, 183*(3), 1199-1215.

NAGY, Z. (1996). Advances in the combined interpretation of seismics with magnetotellurics1. *Geophysical Prospecting, 44*(6), 1041-1083. doi: 10.1111/j.1365-2478.1996.tb00190.x

NAIDU, G. D. (2012). Magnetotellurics: Basic Theoretical Concepts *Deep Crustal Structure of the Son-Narmada-Tapti Lineament, Central India* (pp. 13-35): Springer.

PLANK, T., & LANGMUIR, C. H. (1998). The chemical composition of subducting sediment and its consequences for the crust and mantle. *Chemical geology, 145*(3), 325-394.

POWELL, W., ZHANG, M., O'REILLY, S. Y., & TIEPOLO, M. (2004). Mantle amphibole trace-element and isotopic signatures trace multiple metasomatic episodes in lithospheric mantle, western Victoria, Australia. *Lithos, 75*(1), 141-171.

PRICE, R., GRAY, C., & FREY, F. (1997). Strontium isotopic and trace element heterogeneity in the plains basalts of the Newer Volcanic Province, Victoria, Australia. *Geochimica et Cosmochimica Acta, 61*(1), 171-192.

RAWLINSON, N., & FISHWICK, S. (2012). Seismic structure of the southeast Australian lithosphere from surface and body wave tomography. *Tectonophysics, 572*, 111-122.

RAWLINSON, N., & KENNETT, B. (2008). Teleseismic tomography of the upper mantle beneath the southern Lachlan Orogen, Australia. *Physics of the Earth and Planetary Interiors, 167*(1), 84-97.

RAWLINSON, N., KENNETT, B., SALMON, M., & GLEN, R. (2015). Origin of lateral heterogeneities in the upper mantle beneath South-East Australia from seismic tomography *The Earth's Heterogeneous Mantle* (pp. 47-78): Springer.

RAWLINSON, N., KENNETT, B., VANACORE, E., GLEN, R., & FISHWICK, S. (2011). The structure of the upper mantle beneath the Delamerian and Lachlan orogens from simultaneous inversion of multiple teleseismic datasets. *Gondwana Research, 19*(3), 788-799.

RAWLINSON, N., SALMON, M., & KENNETT, B. (2014). Transportable seismic array tomography in southeast Australia: Illuminating the transition from Proterozoic to Phanerozoic lithosphere. *Lithos, 189*, 65-76.

ROBERTSON, K., TAYLOR, D., HEINSON, G., THIEL, S., STEPAN, M., & SKLADZIEN, P. (2015). MT Traversing the Delamerian and Lachlan Orogens of Victoria to illuminate geological structures, fossil fluid pathways and serpentinisation. *Abstract and Poster, Society of Exploration Geophysics Conference, Hobart*.

ROBERTSON, K., TAYLOR, D., THIEL, S., & HEINSON, G. (2015). Magnetotelluric evidence for serpentinisation in a Cambrian subduction zone beneath the Delamerian Orogen, southeast Australia. *Gondwana Research, 28*(2), 601-611. doi: 10.1016/j.gr.2014.07.013

RODI, W., & MACKIE, R. L. (2001). Nonlinear conjugate gradients algorithm for 2-D magnetotelluric inversion. *GEOPHYSICS, 66*(1), 174-187. doi: 10.1190/1.1444893

ROSSITER, A. (2003). Granitic rocks of the Lachlan Fold Belt in Victoria. *Geology of Victoria*, 217-237.

SELWAY, K., HEINSON, G., & HAND, M. (2006). Electrical evidence of continental accretion: Steeply-dipping crustal-scale conductivity contrast. *Geophysical Research Letters, 33*(6). doi: 10.1029/2005GL025328

SIMPSON, F., & BAHR, K. (2005). *Practical Magnetotellurics*: Cambridge University Press.

SLEEP, N. H. (2009). Stagnant lid convection and carbonate metasomatism of the deep continental lithosphere. *Geochemistry, Geophysics, Geosystems, 10*(11).

SPAGGIARI, C., GRAY, D., FOSTER, D., & MCKNIGHT, S. (2003). Evolution of the boundary between the western and central Lachlan Orogen: implications for Tasmanide tectonics. *Australian Journal of Earth Sciences, 50*(5), 725-749.

SZARKA, L. (1988). Geophysical aspects of man-made electromagnetic noise in the earth—A review. *Surveys in Geophysics, 9*(3-4), 287-318.

TAYLOR, D. H., & CAYLEY, R. A. (2000). Character and kinematics of faults within the turbidite-dominated Lachlan Orogen: implications for tectonic evolution of eastern Australia: discussion. *Journal of Structural Geology, 22*(4), 523-528.

VANDENBERG, A. (1999). Timing of orogenic events in the Lachlan Orogen. *Australian Journal of Earth Sciences, 46*(5), 691-701.

WILLMAN, C., VANDENBERG, A., & MORAND, V. (2002). Evolution of the southeastern Lachlan fold belt in Victoria. *Australian Journal of Earth Sciences, 49*(2), 271-289.

APPENDIX A: MT DEPLOYMENT SUMMARY

Table 1: MT deployment information (GRA01-GRA41). Date of deployment, location (latitude and longitude), elevation and electric dipole length (E_x and E_y) were recorded for all stations and used as inputs during data processing.

Station	Date	Longitude (DD)	Latitude (DD)	Elevation (m)	Length Ex (m)	Length Ey (m)
GRA01	15/06/2016	141.88345	-37.85229	75	50	50
GRA02	15/06/2016	141.9302	-37.838383	192	50	50
GRA03	15/06/2016	141.9736	-37.82203	201	49	50
GRA04	16/06/2016	142.03695	-37.806183	200	49	50
GRA05	15/06/2016	142.09529	-37.79259	226	49	46
GRA07	16/06/2016	142.13644	-37.76468	239	50	50
GRA08	16/06/2016	142.193935	-37.761267	213	47	49
GRA09	16/06/2016	142.25964	-37.75634	220	48.5	48
GRA10A	16/06/2016	142.306217	-37.693217	235	50	49
GRA12	16/06/2016	142.3623	-37.69873	293	47	47
GRA13	16/06/2016	142.41496	-37.66443	325	47	45
GRA14A	17/06/2016	142.471313	-37.621867	256	50	50
GRA16	17/06/2016	142.52875	-37.5988	260	50	50
GRA17	17/06/2016	142.57695	-37.59692	293	46.5	46.5
GRA18A	17/06/2016	142.64235	-37.584117	246	44.5	50
GRA20	18/06/2016	142.701056	-37.556261	253	49	44
GRA21A	17/06/2016	142.78229	-37.53681	256	47	47
GRA23	17/06/2016	142.86147	-37.51759	268	47	45
GRA25A	18/06/2016	142.95581	-37.51152	281	49	47
GRA27	18/06/2016	143.03058	-37.48226	315	48	47
GRA28A	19/06/2016	143.099528	-37.472935	331	50	50
GRA30	19/06/2016	143.159525	-37.435652	338	50	46
GRA31	19/06/2016	143.22067	-37.41623	324	45	48
GRA32A	19/06/2016	143.28233	-37.41461	364	48	48
GRA34	19/06/2016	143.321639	-37.388906	370	50	50
GRA35	19/06/2016	143.38585	-37.37466	485	44	48
GRA36	19/06/2016	143.4406	-37.34867	454	45	45
GRA37	20/06/2016	143.493402	-37.306223	364	48	50
GRA38A	20/06/2016	143.549375	-37.294673	393	50	46
GRA40	20/06/2016	143.617493	-37.272522	376	50	49
GRA41	20/06/2016	143.680088	-37.242378	311	50	50

APPENDIX B: DATA PROCESSING

Table 2: BIRRP spreadsheet parameters used for data processing at 1000Hz. The corresponding UTC day number and start and stop times represent the data window used to process the raw data. Stations used for remote referencing (RR) purposes are also listed.

Station	Freq (Hz)	Day (No.)	Start Time (hh:mm:ss)	Stop Time (hh:mm:ss)	RR Station
GRA01	1000	167	090000	130000	GRA02
GRA02	1000	167	140000	180000	GRA05
GRA03	1000	167	090000	130000	GRA05
GRA04	1000	168	120000	160000	GRA09
GRA05	1000	169	020000	060000	GRA09
GRA07	1000	168	180000	220000	GRA04
GRA08	1000	168	180000	220000	GRA07
GRA09	1000	168	180000	220000	GRA07
GRA10A	1000	168	180000	220000	GRA07
GRA12	1000	169	100000	140000	GRA13
GRA13	1000	169	180000	220000	GRA09
GRA14A	1000	169	120000	160000	GRA13
GRA16	1000	169	120000	160000	GRA13
GRA17	1000	169	120000	160000	GRA13
GRA18A	1000	169	120000	160000	GRA13
GRA20	1000	171	100000	140000	GRA21A
GRA21A	1000	170	140000	180000	GRA20
GRA23	1000	170	140000	180000	GRA21A
GRA25A	1000	170	140000	180000	GRA21A
GRA27	1000	170	140000	180000	GRA21A
GRA28A	1000	171	070000	110000	GRA30
GRA30	1000	171	120000	160000	GRA28A
GRA31	1000	171	120000	160000	GRA28A
GRA32A	1000	171	120000	160000	GRA28A
GRA34	1000	171	120000	160000	GRA28A
GRA35	1000	171	120000	160000	GRA28A
GRA36	1000	172	100000	140000	GRA30
GRA37	1000	172	110000	150000	GRA36
GRA38A	1000	172	110000	150000	GRA36
GRA40	1000	172	110000	150000	GRA36
GRA41	1000	172	110000	150000	GRA36

Table 3: BIRRP spreadsheet parameters used for data processing at 10Hz (decimated data). Corresponding UTC day number and start and stop times represent the data window used to process the raw data. Stations used for remote referencing (RR) purposes are also listed.

Station	Freq (Hz)	Day (No.)	Start Time (hh:mm:ss)	Stop Time (hh:mm:ss)	RR Station
GRA01	10	167	100000	240000	GRA05
GRA02	10	167	100000	240000	GRA05
GRA03	10	167	080000	230000	GRA05
GRA04	10	168;169	060000;000000	240000;200000	GRA09
GRA05	10	168;169	060000;020000	240000;200000	GRA09
GRA07	10	168;169	060000;000000	240000;200000	GRA04
GRA08	10	168;169	060000;000000	240000;200000	GRA04
GRA09	10	168;169	060000;000000	240000;200000	GRA04
GRA10A	10	168;169	060000;000000	240000;200000	GRA04
GRA12	10	168;169	080000;000000	240000;200000	GRA13
GRA13	10	168;169	080000;010000	230000;170000	GRA04
GRA14A	10	169;170	050000;000000	240000;180000	GRA21A
GRA16	10	169;170	050000;000000	240000;180000	GRA21A
GRA17	10	169;170	050000;000000	240000;180000	GRA21A
GRA18A	10	169;170	050000;000000	240000;180000	GRA21A
GRA20	10	170;171	090000;040000	220000;200000	GRA21A
GRA21A	10	170;171	090000;000000	240000;180000	GRA20
GRA23	10	169;170	060000;000000	240000;180000	GRA21A
GRA25A	10	170;171	090000;000000	240000;180000	GRA21A
GRA27	10	170;171	090000;000000	240000;180000	GRA21A
GRA28A	10	171;172	090000;000000	240000;180000	GRA36
GRA30	10	171;172	090000;000000	240000;180000	GRA28A
GRA31	10	171;172	120000;000000	220000;180000	GRA28A
GRA32A	10	171;172	090000;000000	240000;180000	GRA28A
GRA34	10	171;172	090000;000000	240000;180000	GRA28A
GRA35	10	171;172	090000;000000	240000;180000	GRA28A
GRA36	10	171;172	090000;000000	240000;180000	GRA30
GRA37	10	172;173	130000;110000	220000;210000	GRA38A
GRA38A	10	172;173	070000;000000	240000;180000	GRA37
GRA40	10	172;173	070000;000000	240000;180000	GRA38A
GRA41	10	172;173	070000;000000	240000;180000	GRA38A

APPENDIX C: INVERSION MODELLING RESPONSE CURVES

Data fit for the 2D inversion of TE and TM modes for stations GRA02 to GRA40. Plots show apparent resistivity ρ_a (Ωm) and phase ϕ (°) for periods ranging from 0.0064 s to 2184 s. The solid red and blue curves show the response of the inversion model of the TE and TM modes, respectively. The red and blue squares show the original measured MT data of the two modes (TE and TM). RMS values are shown for each station (top right corner).

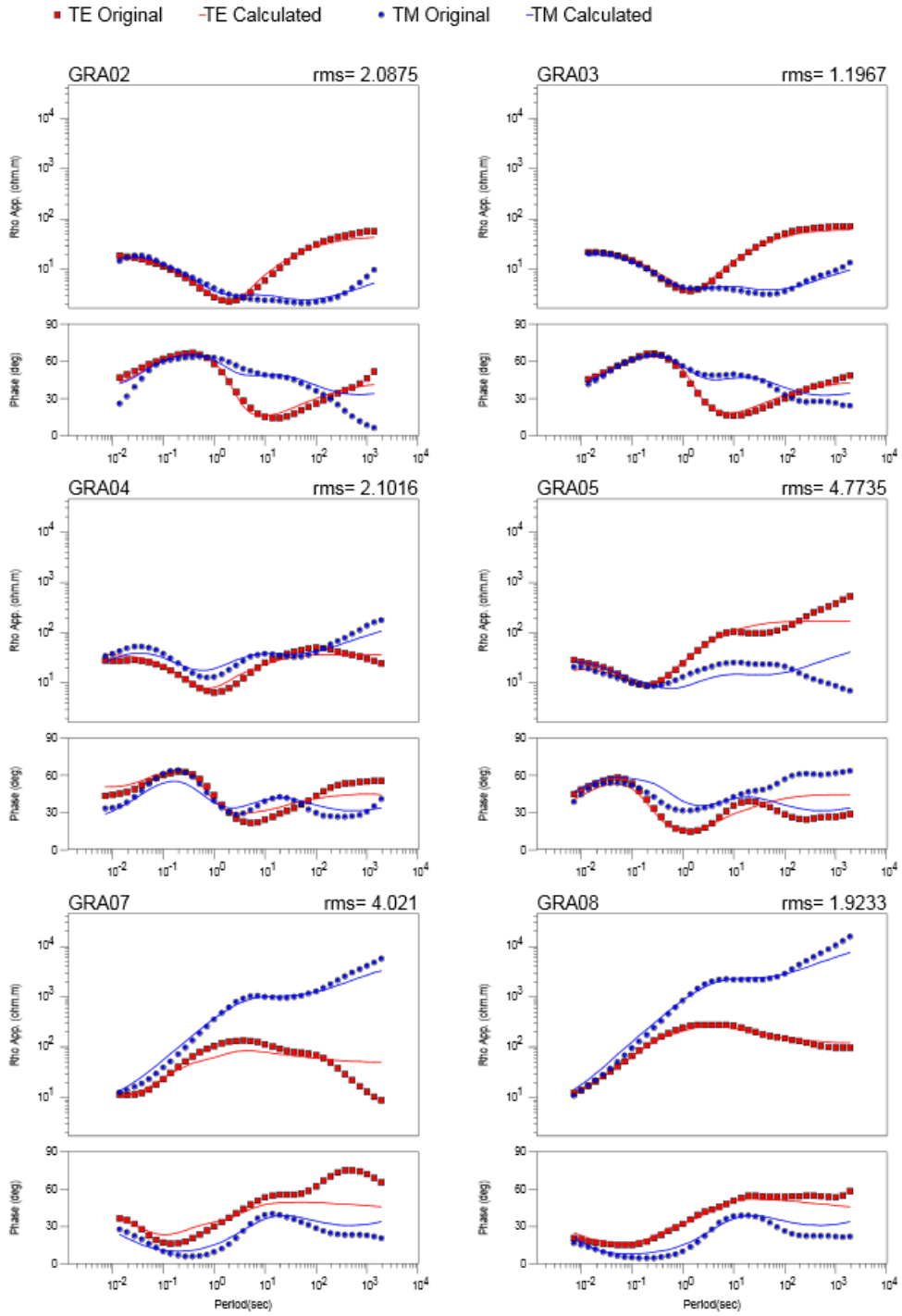

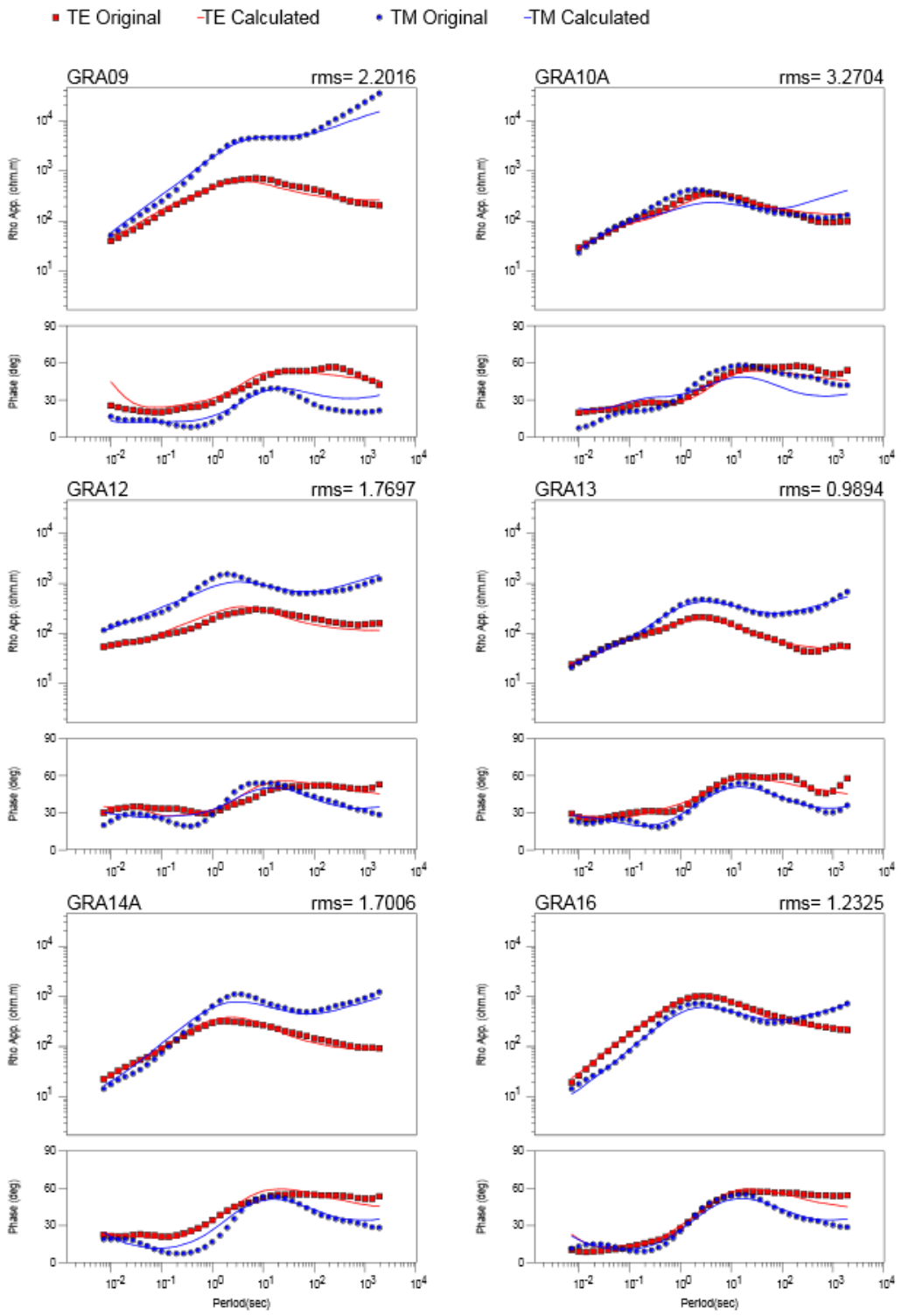
TE Original
TE Calculated
TM Original
TM Calculated
GRA09
rms= 2.2016
GRA10A
rms= 3.2704
GRA12
rms= 1.7697
GRA13
rms= 0.9894
GRA14A
rms= 1.7006
GRA16
rms= 1.2325
Rho App. (ohm.m)
Phase (deg)
Period(sec)

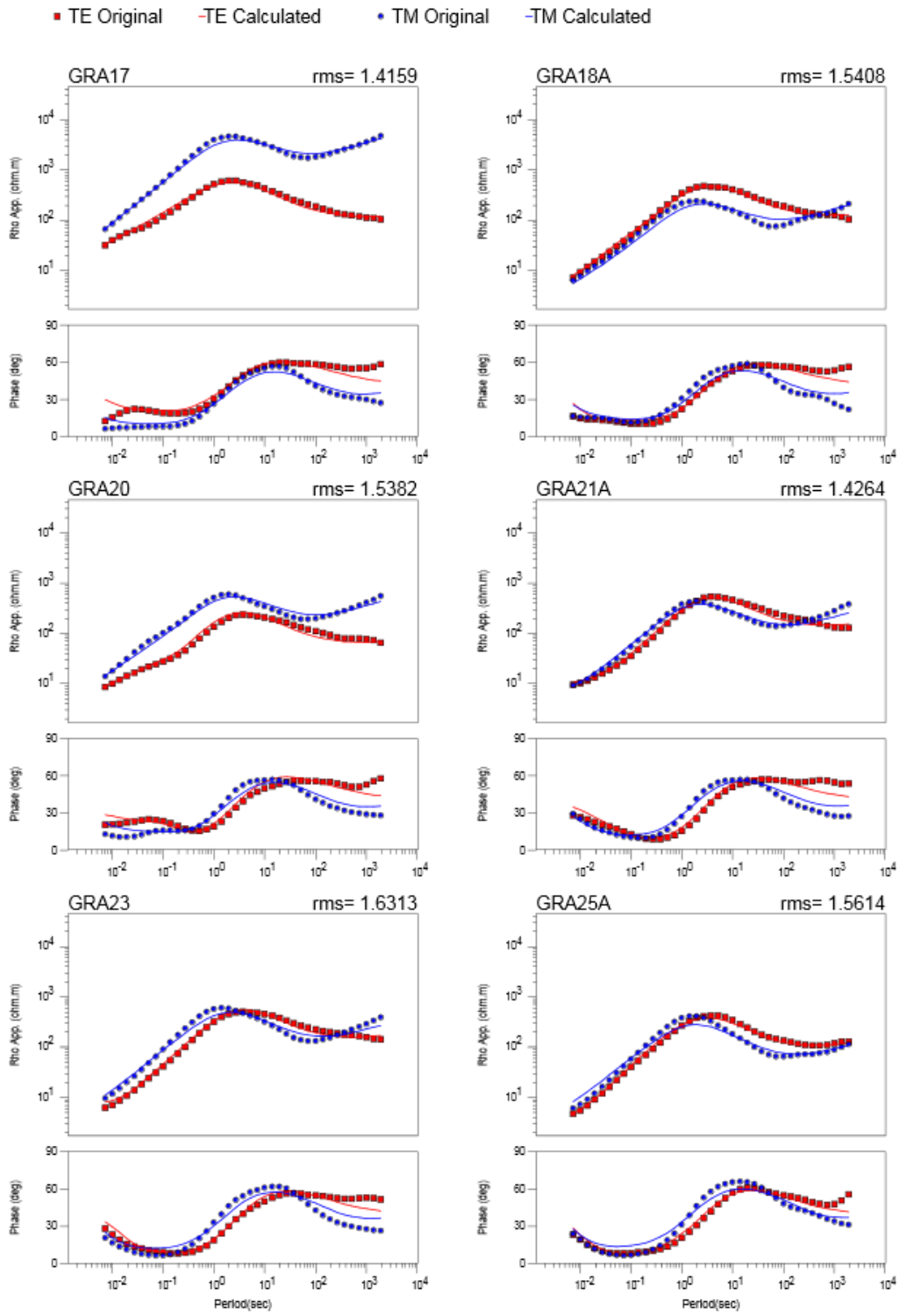
TE Original
TE Calculated
TM Original
TM Calculated
GRA17
rms= 1.4159
GRA18A
rms= 1.5408
GRA20
rms= 1.5382
GRA21A
rms= 1.4264
GRA23
rms= 1.6313
GRA25A
rms= 1.5614
Rho App. (ohm.m)
Phase (deg)
Period(sec)

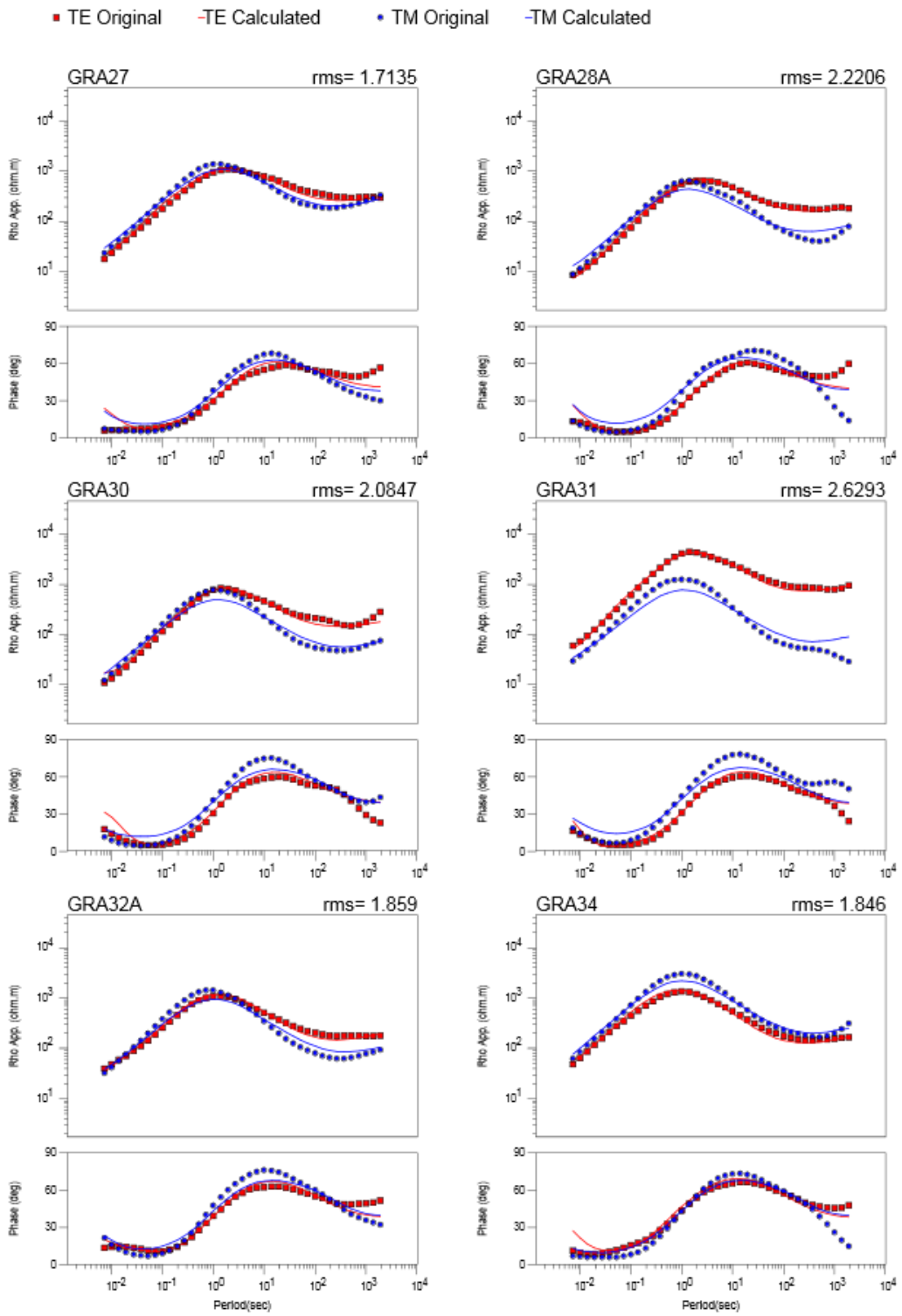
TE Original
TE Calculated
TM Original
TM Calculated
GRA27
rms= 1.7135
GRA28A
rms= 2.2206
GRA30
rms= 2.0847
GRA31
rms= 2.6293
GRA32A
rms= 1.859
GRA34
rms= 1.846
Rho App. (ohm.m)
Phase (deg)
Period(sec)

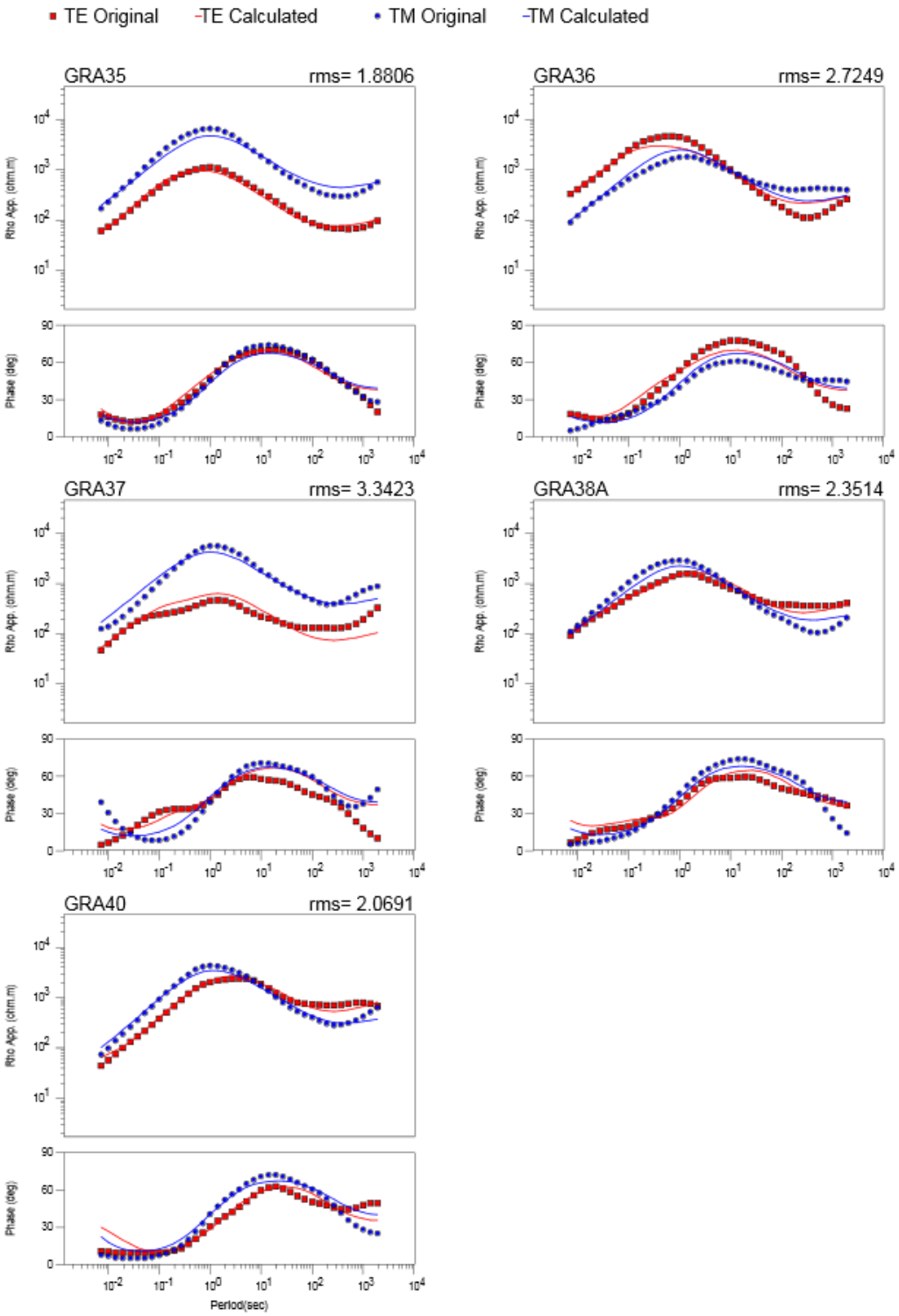
TE Original
TE Calculated
TM Original
TM Calculated
GRA35
rms= 1.8806
GRA36
rms= 2.7249
GRA37
rms= 3.3423
GRA38A
rms= 2.3514
GRA40
rms= 2.0691
Rho App. (ohm.m)
Phase (deg)
Period(sec)